Author version: J. Geophys. Res. (C: Oceans): 114(2); doi:10.1029/2008JC004807, 2009; 18 pp.

Spatio-temporal structure of the East India Coastal Current from satellite altimetry

F. Durand[1,2], D. Shankar[2], F. Birol[3], S.S.C. Shenoi[2]

(1) IRD, LEGOS, UMR5566 CNRS-CNES-IRD-UPS, 14 Avenue Edouard Belin, 31400 Toulouse, France

(2) National Institute of Oceanography (Council of Scientific and Industrial Research), Dona Paula, Goa 403004, India

(3) Center for Topography of Oceans and Hydrosphere, LEGOS, UMR5566 CNRS-CNES-IRD-UPS, 14 Avenue Edouard Belin, 31400 Toulouse, France

Corresponding author : Fabien Durand (fabien.durand@ird.fr)

Manuscript accepted for publication in Journal of Geophysical Research
Published in Vol. 114, C02013, doi:10.1029/2008JC004807, 2009

Abstract

We use a newly processed altimeter data set to present a hitherto unprecedented description of the spatio-temporal structure of the East India Coastal Current (EICC): the data set resolves time scales ranging from a few months to a few years, and the high along-track resolution yields the first description of the cross-shore structure of the current. The seasonal cycle dominates the variability, but the non-annual time scales have similar energy levels all along the EICC path. There are short-lived, intense intraseasonal bursts. In contrast to the seasonal cycle, the interannual and intraseasonal components are decorrelated along the coast, and possible mechanisms for the decorrelation (discontinuity in the flow) are discussed. In the cross-shore direction, the current is highly correlated at all time scales: The EICC is trapped against the shelf, with the current offshore flowing in the opposite direction at most locations. The EICC appears as an inherently discontinuous flow, taking the form of a few recirculating loops along the EICC path, with a typical cross-shore spatial scale of 150–200 km. The loops are highly variable in direction at all time scales from intraseasonal to interannual. This discontinuity of the EICC in space and time implies that the basic pathways and advective time scales for the inter-basin exchange of water masses between the Bay of Bengal and the Arabian Sea are not robust when the full spatio-temporal variability of the EICC is considered.

1. Introduction

The East India Coastal Current (henceforth EICC) is the western boundary current of the Bay of Bengal (Figure 1). Forming a part of the monsoon-current system that reverses twice a year under the influence of alternating monsoons, the EICC participates in the exchange of water masses between the Arabian Sea and Bay of Bengal [e.g. *Shetye et al*., 1996; *Shankar et al.*, 2002; *Durand et al*., 2007], thereby playing a crucial role in maintaining the large-scale hydrological balance between the Arabian Sea (a concentration basin) and the Bay of Bengal (a dilution basin). In turn, these water mass exchanges are expected to play a role in the region's climate [*Shenoi et al*., 1999a; *Vinayachandran et al*., 2007, and references therein].

Despite its climatic interest, the western boundary of the Bay of Bengal suffers from a severe lack of oceanographic observations. The ship-drift climatologies assembled by *Cutler and Swallow* [1984] and *Mariano et al.* [1995] reveal — though at a coarse resolution — a well-organized structure of the EICC in space and time, at seasonal time scales. In November, the EICC flows equatorward all along its path, but it reverses everywhere north of 10°N by February (Figure 2). It strengthens during March–May, well before the onset of the southwesterlies associated with the summer monsoon. South of 10°N, on the southeast coast of Sri Lanka, the timing is somewhat different: the current remains southwestward until April, thereby feeding the westward-flowing Winter Monsoon Current (WMC). The two currents reverse in May to flow poleward and eastward respectively. In June, as the summer monsoon sets in, the northward-flowing EICC decays in the north. By August, it collapses everywhere north of 10°N. In September, it starts flowing equatorward everywhere north of 10°N. Based on a series of three dedicated hydrographic surveys encompassing the peak summer monsoon, pre-summer monsoon and winter monsoon periods, *Shetye et al.* [1991, 1993, 1996] confirmed the coarse picture initially drawn from the ship-drift data.

Shetye et al. [1991] had attributed the shallow poleward EICC (with an equatorward undercurrent) during the summer monsoon to the local alongshore winds, drawing an analogy with the classical eastern boundary currents. The strong western boundary current of the seasonal subtropical gyre, seen during March–May, was attributed to Ekman pumping in the Bay of Bengal [*Shetye et al*., 1993], drawing an analogy with the classical subtropical gyres of the Atlantic and Pacific Oceans.

This picture changed completely in the 1990s, when it was shown that remote forcing from the equatorial Indian Ocean has a significant impact on the circulation in the Bay of Bengal, including the seasonal cycle of the EICC [*Potemra et al*., 1991; *Yu et al.*, 1991]. The winds over the equatorial Indian Ocean generate Kelvin waves that, on reflecting at the eastern boundary, trigger

coastal Kelvin waves that propagate all around the rim of the bay. *McCreary et al*. [1993] (henceforth MKM93) confirmed the importance of equatorial winds, but showed that Ekman pumping over the interior of the bay as well as alongshore winds off the Indian east coast are important. Using a continuously stratified linear model of the Bay of Bengal circulation, *Shankar et al*. [1996] and *McCreary et al*. [1996] quantitatively analyzed the four linear forcing mechanisms of the seasonal EICC: local forcing by the alongshore winds; Ekman pumping in the interior bay and associated westward-propagating long, baroclinic Rossby waves; remote forcing from the northern and eastern boundaries of the bay; and remote forcing from the equatorial Indian Ocean. They concluded that each of the four mechanisms has a significant influence on the EICC variability at some time during the year. Overall, Ekman pumping in the interior basin and local alongshore winds seem to play the prominent role [*Shankar et al*., 1996], with the other two processes influencing the EICC mostly during the transition seasons when it reverses direction [*McCreary et al*., 1996]. *Vinayachandran et al*. [1996] confirmed these findings using an oceanic general circulation model. Using both complex and simple numerical models, *Shankar et al*. [2002] concluded that the dynamics of the seasonal EICC, as also that of the rest of the monsoon currents system in the northern Indian Ocean, is essentially linear.

At interannual time scales, our knowledge of EICC variability is limited. Coastal sea-level variations have been linked to interannual variations in the equatorial zonal wind [*Clarke and Liu*, 1994] and interior Ekman pumping over the bay [*Han and Webster*, 2002]. The Indian Ocean Dipole (IOD) [*Reverdin et al.*, 1986; *Murtugudde et al.*, 1998, 2000; *Saji et al*., 1999; *Webster et al*., 1999], a coupled ocean-atmosphere event that occurs every few years and lasts about 6 months, also impacts the bay [*Rao et al*., 2002; *Jensen*, 2007], as does ENSO (El Niño and Southern Oscillation) [*Srinivas et al*., 2005]. Another key forcing comes from variability in freshwater flux, which impacts sea level along the east coast of India and hence the EICC at seasonal [*Shankar*, 1998, 2000; *Han et al.*, 2001; *Han and Webster*, 2002], interannual [*Han and Webster*, 2002], and longer [*Clarke and Liu*, 1994; *Shankar and Shetye*, 1999] time scales. For example, the mean-sea-level difference between the east and west coasts of India [*Shankar and Shetye*, 2001] is as strongly influenced by salinity as by the wind field.

The lack of observations becomes even more serious at intraseasonal time scales. Hydrographic surveys [*Shetye et al*., 1991, 1993, 1996; *Sanilkumar et al*., 1997; *Babu et al*., 2003], surface drifter trajectories [*Shenoi et al*., 1999b], and eddy-resolving numerical models [*Vinayachandran et al*., 2005] show that, irrespective of the season, the EICC has several mesoscale structures, which typically take the form of cyclonic and anticyclonic recirculation cells with a scale of about 200 km. Though altimetric sea level provides an opportunity to describe such meso-scale

features and the associated EICC at time scales varying from a few weeks to a few years, the standard gridded products are too coarse for this purpose. They also suffer from heavy loss of data near the coast, with errors being particularly large within the boundary-trapped regime of the EICC [*Han and Webster*, 2002; *Durand et al.,* 2008, herefater referred to as D08].

As demonstrated by D08, however, newly developed processing techniques [*Birol et al*., 2006] have overcome most of these issues, making it possible to use satellite altimeter data to study the variability of boundary currents like the EICC. In this paper, we have made use of the specially reprocessed altimeter sea-level data to provide an observational, synoptic description of EICC variability at the surface from intraseasonal to interannual time scales. Specifically, we use the processed along-track data from the altimeter, avoiding the spatial smoothing inherent in a gridded data set. The tracks used intersect the east coasts of India and Sri Lanka (Figure 1), thereby sampling the entire regime of the EICC. We show that the seasonal cycle dominates the EICC over its entire length, but non-seasonal (interannual and intraseasonal) variations are significant. As expected from earlier studies, the seasonal EICC is well correlated along the coast, but we show that the non-seasonal variations are not coherent along the coast.

The paper is organized as follows: Section 2 describes the data set and method of analysis, Section 3 presents the seasonal variability of the EICC, Section 4 presents the non-seasonal variability, Section 5 depicts the EICC structure in the cross-shore direction, and Section 6 discusses the reasons for the lack of alongshore correlation of the non-seasonal EICC variability. Section 7 concludes the paper.

2. Data and methods

2.1 Data processing

This study is essentially based on an analysis of the recently released coastal altimetric data set presented in *Birol et al*. [2006]. The reader is referred to this paper and the references therein for further details. In brief, it consists of TOPEX/Poseidon (T/P hereafter) MGDR (Merged Geophysical Data Records) data re-processed using a processing chain specially developed for marginal seas, the MAP (Margins Altimetry Project) processing. The main problems of altimetry in the shelf areas arise from data accuracy, which is partly due to the lack of resolution of the standard geophysical corrections (tidal and de-aliasing of global high-frequency barotropic motions), and the data gaps near the coast. Consequently, the near-coastal data are often flagged (out) in standard products. Recent studies have shown that a careful analysis of both measurements and corrective terms permits the recovery of valid measurements in the coastal domain [e.g. *Vignudelli et al.,* 2000]. The MAP processing involves an ad-hoc editing strategy of the data records, and a careful

extrapolation/interpolation of missing or defective corrective terms of the altimetric measurements in the coastal strip. Tidal corrections are derived from the higher-accuracy FES2004 model [*Lyard et al*., 2006]; the ocean high-frequency atmospheric-forcing response corrections are derived from the MOG2D_G model [*Carrère and Lyard*, 2003]. The result is high-resolution along-track sea-level-anomaly (SLA) data.

We post-processed the MAP coastal altimetric SLA data set to retrieve the coastal surface current anomaly in the cross-track direction. Following D08 (see their Section 4 for a comprehensive description and validation of the processing algorithm), we spatially smoothed the along-track raw SLA profiles prior to computing the cross-track surface geostrophic current anomaly by the usual geostrophic relation. The reason for this smoothing is that the velocity field is expected to adjust to the density field (and therefore to sea level) only at scales larger than the Rossby radius of deformation (denoted by *Ro* in the rest of this manuscript). We applied this method to the set of T/P tracks along the EICC path (Figure 1) for the period 1992–2002.

We considered only the T/P tracks sufficiently orthogonal to the shelf break, that is the tracks intersecting the 200 m isobath at an angle greater than 45°. Under this condition, the boundary current projects more on the cross-track direction than on the along-track direction; hence the determination of the alongshore current from along-track SLA is favourably conditioned. From north to south, the corresponding tracks are labelled #14, #192, #116, #40, #155, and #218. In the subsequent analyses, however, one must keep in mind that Track #155 and Track #218, which intersect the 200 m isobath at an angle slightly greater than 45°, are not sufficiently oriented in the cross-EICC direction; as a result, care should be taken when interpreting the derived geostrophic, alongshore current. In the rest of the paper, we refer to the cross-track current for all the six T/P tracks as the "alongshore current." Track #142 is not strictly within the EICC path but is of interest for two reasons. First, it provides insight into the connection between the EICC and its southern outlet, the WMC or the Summer Monsoon Current (SMC). Indeed, past studies have revealed that the monsoon current south of Sri Lanka has a close dynamical link with the EICC, the two currents forming a continuous flow during some part of the seasonal cycle [*Schott and McCreary*, 2001; *Jensen*, 2001; *Shankar et al*., 2002], which, in turn, has implications for the thermodynamics of the south-eastern Arabian Sea [*Shenoi et al*., 1999a; *Durand et al.*, 2007]. Second, Track #142 is very close to the section along 80°30'E, where currents were monitored by in situ current meters [*Schott et al.*, 1994]. To our knowledge, these are the only long-term records of ocean currents reported so far from the region. Hence, though the T/P period (November 1992 onwards) does not encompass the in situ measurements period (January 1991 to March 1992), it permits a consistency check on the basic features of the current retrieved from the two independent data sets.

The data coverage for the seven tracks is shown in Figure 3. We can see that our data set permits monitoring the variability of the boundary current to within about 50 km of the coast, which is the typical location of the shelf break for Tracks #192, #116, #40, #155, and #218. The gappiest time series are found at the shoreward edge of Tracks #14 and #155 and at the southern edge of Track #142, with gaps as long as 2–3 months occurring on a few occasions. For the rest of the data set, the data gaps typically do not exceed one month (three T/P cycles). Hence, periods ranging from about 2 months to 3–4 years are adequately resolved. The dataset is available at http://www.legos.obs-mip.fr/en/soa/.

2.2 The raw current

For each track, we selected the point of maximal variability of the cross-track current. These points are labelled A to G in Figure 1, from the northernmost section (Track #14) to the southernmost one (Track #142); their precise positions are given in Table 1. We refer to them as the "EICC points" in the rest of the manuscript. Figure 4 presents the raw, or unfiltered, time series of the current we retrieved (geostrophic anomaly only, as the Ekman component and the geostrophic mean current were found to be negligible). We superimposed the seasonal climatology of the current (computed as a simple monthly average of the long-term time series) for perspective. In agreement with the seasonal variability of EICC known from past studies (see Section 1), the seasonal features are evident even in the raw current throughout the record. For instance, at Point C, the reversal of the current from equatorward to poleward occurs in early January in most of the years; similarly, at Point F, the same reversal occurs always in April. The year-to-year variability, however, is considerable, taking the form of short-lived (typical duration was a few weeks), intense (of order 1 m s^{-1}) bursts: for example at Point A in early 1998, the EICC speed exceeded 70 cm s^{-1} in January and February. We show later that these bursts of the surface current are not restricted to the EICC points we selected, but spread over a strip extending offshore for several tens of kilometres.

The year-to-year variability of the raw, unfiltered EICC is not correlated along the western boundary of the bay (Table 2): the point-to-point correlation is low, and only pairs of neighbouring points show significant correlations. The highest point-to-point correlations are observed between the two southernmost points, along the southern coast of Sri Lanka, where the current variation is relatively similar between Points F and G, even though the numerous gaps in the current time series at Point G blur the picture displayed in Figure 4.

Figure 5 presents the Lomb periodogram, computed using the algorithm described by *Press et al.* [1992], of the current variability for these points. The presence of gaps in the time series precludes use of standard Fourier analysis. All the EICC points exhibit a spiked structure of the

periodogram, with a large part of the variability concentrated at the statistically significant annual frequency. This band of variability is designated as "annual" or "seasonal' time scale in the rest of this paper. All the points also show secondary peaks of significant variability, though of lesser amplitude, and at varying time scales (60 days for point A, 6 months for points B, D, and G, 3–4 years for point C, 2 years for point E, and 4 months for point F). For the four northernmost tracks, the secondary peak clearly exceeds the 95% significance level; for the three southernmost tracks also, the secondary peak just exceeds the 95% level, but this secondary peak in the south is not as conspicuous as in the north. As expected from Figure 4, these results do not mean that the EICC we monitor has negligible variability at frequencies other than the annual; rather, it means that over the 10-year-long period that we have analyzed, the annual periodicity is, by far, the most consistent, at every location. Since the seasonal cycle is also the best described and understood aspect of the EICC's variability, we begin our analysis by comparing "our" seasonal EICC with existing data.

3. The seasonal EICC

3.1 The climatological seasonal cycle

The seasonal climatology of the retrieved EICC (corrected from the Ekman drift) is shown in Figure 6. We note two issues with the data set. First, altimetry allows monitoring of only anomalies of the geostrophic surface current with respect to the long-term mean. We did not take into account the long-term mean surface current in our analysis. Based on *Levitus and Boyer* [1994] and *Levitus et al.* [1994] (henceforth Levitus) hydrographic climatology, *Shankar et al*. [2002] showed that it is negligible (of order 1 cm s^{-1}) over most of our domain, but not negligible for Point G (westward mean current, of about 10 cm s^{-1}). As noted by *Shankar et al*. [2002], the Levitus grid is coarse, implying that the above estimates of the mean geostrophic current (although the best currently available for this region), underestimate the mean EICC. In addition, the magnitude of the EICC for Point E and Point F may be underestimated owing to the non-perpendicular layout of these T/P tracks with respect to the shelf break (see Section 2). Nevertheless, having no information about the flow component parallel to the track, we did not make any attempt to correct for this possible bias in the estimated EICC magnitude. Neither issue, however, precludes the analysis that follows. Indeed, as we will show, the data set is rich enough to permit an unprecedented description of the EICC variability.

Our estimate is consistent with the ship drifts of *Mariano et al.* [1995] (Figure 6). Among the few notable discrepancies is Point G, where the ship-drift SMC south of Sri Lanka shows a relative minimum in July, occurring between two maxima in June and September, whereas our product shows a smooth dome-like evolution, reaching its maximum in July. The reason for this difference is

not clear. For all the locations, over the entire seasonal cycle, the Ekman drift is weak (typically less than 10 cm s^{-1}) as compared to the variability of the geostrophic flow. Only for the two southernmost points south of Sri Lanka (F and G) does it exceed 15 cm s^{-1} during the peak of the summer monsoon.

3.2 The cross-shore structure

To reveal the spatial extent (in the cross-shore direction) of the seasonal variability of the EICC we just described, we extended the computation of the Lomb periodogram to the whole set of altimetric points along each track. As in D08, to enable a comparison of the spectral power among the different altimetric points on a given track, we did not normalize the Lomb periodogram by the overall variance of the time series (see *Press et al*. [1992]). Figure 7 presents the resulting non-normalized Lomb power of the annual component of the time series for each track. For the central and southern parts of the western boundary (from north to south: Tracks #192, 116, 40, 155, and 218), the annual variability of EICC is trapped at the shelf break, consistent with the linear theory [*Shankar et al*., 1996]. The *e*-folding scale of the annual power in the cross-shore direction (Table 3) is not strictly in agreement with the theoretical value of *Ro*/2 expected from linear theory, implying that non-linear dynamics might play a role in the observed cross-shore structure of the western boundary current. Nevertheless, the property that the observed trapping scale increases equatorward, as does *Ro*, suggests that linear dynamics at the shelf break is still relevant to explain, at least partly, the observed EICC trapping. At the northernmost extremity of the EICC (Track #14), most of the energy is trapped on the shelf, not at the shelf break, possibly because the shelf is much wider there than at other locations along the coast (Figure 1). That the energy along Track #142 is relatively weak at its northern edge against the shelf off the tip of India, unlike along the tracks on the east coasts of India and Sri Lanka, could indicate that the current deviates offshore once it reaches the southern tip of Sri Lanka because of the curvature of the coast there [*Clarke,* 1977].

3.3 Alongshore correlation

In order to isolate the annual frequency in the multi-year record of the current we retrieved, we applied two successive filters to the raw time series: one low-pass Hanning filter of 250 days, and one high-pass Hanning filter of 500 days. The residual obtained after the application of both the filters is considered the annual component of the current. The filtering was done after the data gaps in the time series were filled by linear interpolation in time.

Table 4 presents the point-to-point correlation of the annual EICC. Unlike the unfiltered EICC (see Section 2), as might be expected from the coherent (along the coast) sea-level variations at the seasonal time scale [*Shankar*, 1998, 2000], the seasonal variability of the surface EICC is also

significantly correlated, but in two separate regions: north of 15°N (Points A, B, and C) and between 5°N and 10°N (Points E, F, and G). This separation is in agreement with earlier observational [*Eigenheer and Quadfasel*, 2000; *Shankar*, 2000] and modeling [*Shankar et al*., 1996; *McCreary et al*., 1996] studies of the EICC, and is due to the sharp change seen in Ekman pumping field in the interior Bay of Bengal across ~ 12°N.

4. The non-seasonal EICC

4.1 Deviation from the seasonal cycle

The seasonal climatology of the EICC accounts only for about one-third to two-thirds of the total variance exhibited by the raw time series (Figure 6), despite the periodograms exhibiting a prominent spike at the annual frequency (Figure 5), so that a significant (Points B, E, and F) or even dominant (Points A, C, D, and G) part of the EICC variability occurs at time scales other than the annual. Figure 6 presents the non-seasonal envelopes of the EICC (defined by plus or minus one standard deviation of the EICC anomaly around the seasonal climatology). For all the points along the EICC path, the standard deviation of the current around its seasonal climatology is ~ 0.6 m s^{-1}, greater than the standard deviation of the seasonal climatology itself. Hence, consistent with what was seen in Figure 4, not only the magnitude of the current, but even its direction (poleward or equatorward), is not a robust feature of the EICC. One exception concerns the three southernmost EICC points (E, F, and G) during winter, when the equatorward (Point E in November–December and Point F in December) and westward (Point G in December–January) direction of the flow is more robust, even though the non-seasonal standard deviation is of the same order as the seasonal flow itself.

4.2 Interannual variability

In accordance with the spectral analysis of Section 2, the interannual component of the EICC, obtained by applying a low-pass Hanning filter of 500 days (see Section 3.2) is weak (Figure 8) for the two southernmost points (F and G). Visual inspection of the time series at various locations along the EICC path confirms that its interannual variability is not structured at large spatial scales. This is illustrated in Figure 8 for two particular dates in August 1996 and May 1997, which are representative of this feature over the entire record. Unlike the seasonal cycle, the alongshore correlation is weak for the interannual EICC (Table 5). The maximal amplitude is seen in the central region (point D), with peak-to-peak variations of ± 0.5 m s^{-1}.

4.3 Intraseasonal variability

The intraseasonal component of the EICC, obtained by applying a high-pass Hanning filter of 250 days (see Section 3.2), is shown in Figure 9 for 1999. It is representative of the entire 1993–2002 period. Intraseasonal variability is marked throughout the period, with no apparent seasonality in the bursts; this lack of seasonal dependence is in accordance with the in situ measurements of *Schott et al.* [1994] close to Point G. The magnitude and the typical duration of the current bursts were consistent with the current-meter observations of *Schott et al*. [1994; see their Figure 2a].

As with the interannual component, there exists no apparent relation between the intraseasonal variability at the various EICC points (Table 6): the variability is discontinuous along the western boundary of the bay. Possible reasons for this discontinuity of the flow at intraseasonal (as well as at interannual) time scales are discussed in Section 6.

4.4 EICC and IOD variability

A key component of interannual variability in the Indian Ocean is the IOD [e.g. *Saji et al*., 1999; *Webster et al.*, 1999]. Rao *et al.* [2002] investigated the signature of IOD activity in the upper-ocean circulation of the Bay of Bengal using gridded T/P data and a numerical model. They concluded that in their model, the basin-scale circulation around its rim is anomalously anticyclonic (hence EICC anomalously poleward) during the fall season of positive IOD years, a result confirmed by *Thompson et al*. [2006] and *Jensen* [2007]. Figure 10 presents the evolution of the anomaly (with respect to the monthly climatology of Figure 6) of our EICC, along with the evolution of the Dipole Mode Index (DMI) defined by *Saji et al*. [1999]. It only partially confirms the previous studies: during the fall 1994 IOD event, only Points A, D, and E showed a significant poleward anomaly of the EICC; during the fall 1997 IOD event however, the EICC was anomalously poleward throughout our domain. Overall, during 1993–2001, the interannual EICC did not obviously follow the DMI variability at any of our reference locations.

5. Cross-shore structure of the EICC

Even though the EICC appears as a succession of short-lived bursts, the along-track correlation of the current is high (Figure 11), revealing a cross-shore structure that does not differ from that of the seasonal cycle (Figure 7). Like the annual response, the variability is still boundary-trapped within one *Ro*, as in the hydrography of *Shetye et al*. [1991, 1993, 1996], implying that a significant part of the EICC variability can be explained by linear wave theory [*Potemra et al*., 1991; *Yu et al*., 1991; MKM93; *Shankar et al*., 1996; *McCreary et al*., 1996; *Vinayachandran et al.*, 1996].

In contrast, there is also a significant *anticorrelation* between the EICC and the offshore cross-track current north of 15°N (Tracks #192, #116, and #40). As shown in D08, there is a quasi-permanent shear between the EICC and the offshore current, characteristic of a recirculating loop. The typical cross-shore extent of these loops is 150–200 km.

To exploit the high information content in both space (cross-shore) and time of our data set, we subjected the raw time series to an empirical orthogonal functions (EOF) analysis; we used the algorithm of *Toumazou et al*. [2001] to perform the decomposition. The dominant EOF mode for each track is shown in Figure 12. Except for Track #14, for which the first EOF mode explains only 43% of the variance, a significant part (half to two-thirds) of the variance could be explained by just one mode. For all tracks, this dominant mode has a spatial structure similar to the spatial correlation functions of Figure 11. For Points B to F, the magnitude of the dominant EOF mode is maximum at the shelf break, decaying offshore with an *e*-folding scale of same order as *Ro*. Between 15°N and 20°N (Tracks #192, #116 and #40), in accordance with Figure 11, the dominant mode exhibits a shear between the shelf break, where the EICC is trapped, and the region 150–200 km offshore. This shear is again a signature of the quasi-permanent recirculation associated with the boundary current. For Track #14, the dominant mode shows a maximum of energy at point A on the shelf in the northern bay. For Track #142 southwest of Sri Lanka, the leading EOF mode confirms that the variability of the current is no longer boundary-trapped. The time function associated with the first EOF mode of each track presents a broad spectrum of variability, comparable to that of the raw EICC (Figure 4), with short bursts with a typical duration of two months superimposed on lower frequency variations (seasonal to interannual periodicities).

Extension of the EOF decomposition to the three spectral components of the current previously defined (intraseasonal, annual, and interannual), showed that the spatial function of the leading EOF mode is robust throughout the spectrum for each track, with a trapping of the current variability within about one *Ro* off the shelf break, and a reversal farther offshore (see auxiliary material, Figure S1). This similarity across the range of time scales suggests that the same basic linear dynamics highlighted at seasonal time scales in the previous modelling studies plays a role in the low-frequency modulation of the current seen at interannual time scales and in the bursts observed at intraseasonal time scales. This coherence in the cross-shore direction is not seen, however, in the alongshore direction: consistent with the weak point-to-point correlation of the EICC (Table 2), there is no similarity between the leading EOF time functions for the different tracks.

Thus, from this analysis, the western boundary circulation of the Bay of Bengal appears as a juxtaposition of several independent recirculating loops hugging the western boundary of the bay, the EICC forming the western arm of these loops.

6. Alongshore decorrelation: Possible mechanisms

It is only the seasonal EICC that is coherent along the coast. In striking contrast to this alongshore coherence in the annual component of the EICC (Table 4), the interannual (Table 5) and intraseasonal (Table 6) currents are decorrelated and therefore discontinuous along the coast. The cause of this difference between the seasonal and non-seasonal EICC is not obvious, given that the EICC is forced at all time scales by the same mechanisms, namely, local alongshore winds, remote forcing due to Ekman pumping over the interior bay, remote forcing due to alongshore winds off the northern and eastern boundaries of the bay, remote forcing from the equatorial Indian Ocean, and local western-boundary turbulent dynamics [MKM93; *Shankar et al.,* 1996; *McCreary et al.*, 1996]. Clearly, given the high values of the current observed on many occasions (Figure 4), the turbulence is expected to trigger eddies (through baroclinic and/or barotropic instability) in our area. In turn, these eddies are bound to contribute to the observed discontinuity of the EICC along its path. To assess quantitatively the role of each of the forcing processes requires numerical experiments that are beyond the scope of the present paper. Therefore, we discuss here only the possible role of mechanisms that might account for the observed discontinuous pattern of the flow at both interannual and intraseasonal time scales; as in *Shankar et al.* [1996], we restrict our analysis to the processes amenable to analytic treatment.

6.1 Discontinuous interannual EICC

The interannual variability of the local alongshore wind (from ERS wind data) is negligible in comparison to that of the seasonal and intraseasonal variability (not shown). Hence, this mechanism can be ruled out as a possible cause of the discontinuity in the observed flow.

Following *Kessler and Gourdeau* [2007] (henceforth KG07), we investigated the role of interior Ekman pumping using a linear, reduced-gravity, Rossby-wave model of the Bay of Bengal. In this model,

$$\frac{\partial h}{\partial t} - \frac{\beta c^2}{f^2}\frac{\partial h}{\partial x} + Rh = -curl(\frac{\tau}{\rho f}), \qquad (1)$$

where h is the pycnocline depth anomaly, f is the Coriolis parameter, β its meridional derivative, R a damping coefficient (taken to be 24 months^{-1} as in KG07), τ the wind stress, ρ the density and c the gravity wave speed, which we assumed to be 2.64 m s^{-1} [following *Shankar et al*., 1996].

As in KG07, we discarded the potential influence of signals radiating westward from the eastern boundary of the domain; such signals would be generated by winds blowing along this boundary and/or by waves emanating from the equatorial waveguide. It follows from this assumption

that the solution to Equation (1), at each latitude, is the integral of the forcing along the Rossby wave ray (weighted by the damping factor) from the eastern boundary. Hence,

$$h(x,t) = -\frac{1}{c_r}\int_{x_E}^{x} \exp[-\frac{R}{c_r}(x-x')] \left[\frac{\tau(x', t-\frac{x-x'}{c_r})}{\rho f}\right] dx', \qquad (2)$$

where $c_r = -\frac{\beta c^2}{f^2}$ is the Rossby wave speed and x_E is the longitude of the eastern boundary. In practice, we define the limits of our domain by the position of the 200 m isobath, from 6°N (the latitude of the southern tip of Sri Lanka) to 20°N (the northernmost position of the 200 m isobath in the Bay of Bengal). An estimate of the western boundary transport generated by this solution can then be made, assuming that the interior flow is geostrophic and that the western boundary flow is simply the flow needed to balance the cross-shore interior flow (see *Godfrey* [1975] and KG07 for further details).

In our case, given that the basin is closed at its northern boundary, the western boundary transport (in the alongshore direction) is null at the northern extremity of the domain, and the general solution is given by

$$V(y) = \int_{y}^{y_N} \frac{c^2}{f}\frac{\partial h_{RW}}{\partial y'} dy', \qquad (3)$$

where h_{RW} is the solution of the Rossby wave model given by Equation (2) at the westernmost point of the domain; the integral in Equation (3) is computed following the (curvilinear) western boundary. We computed the solution only for EICC Points B to F because Point A is north of the relevant domain and Point G lies outside the western boundary regime.

The resulting western boundary transport was filtered in the same way (low-pass Hanning filter) as the altimetric current in order to isolate its interannual component. The low-passed western boundary transport generated by the reduced-gravity Rossby wave model has a standard deviation ranging from 0.1 Sv at Point B to 0.4 Sv at Point F, comparable to the variability of the total interannual EICC. The correlation matrix of the interannual western boundary transport driven by interior Ekman pumping (Table 7) shows that this mechanism contributes to the discontinuous flow at this time scale. This is particularly so for Points C, D, and E, which exhibit the strongest EICC interannual variability. This discontinuity can be explained by the short meridional scales of the interannual Ekman pumping velocity (see auxiliary material, Figure S2).

As for the remote forcing (from the equatorial Indian Ocean as well as from the eastern and northern boundaries of the bay), as discussed by *Clarke and Liu* [1994], given the small size of the basin, the western boundary should be in quasi-equilibrium with the forcing. Indeed, the slowest mode-1 Rossby wave takes no longer than six months to cross the entire basin, and the boundary-trapped Kelvin waves are even faster to adjust the ocean all along the periphery of the bay. Hence, it is expected that the associated sea-level variability in the Bay of Bengal should be roughly uniform at interannual time scales; in turn, the associated EICC variability should be uniformly weak all along its path. Still, these theoretical considerations need to be checked with a dedicated modeling approach.

The role of nonlinearities in the observed discontinuity of the interannual EICC is not clear. It also calls for a model study, as does the buoyancy forcing by freshwater flux from the continent, which has been invoked earlier to explain the pattern of low-frequency variability of coastal sea level, and hence of the EICC [*Shankar and Shetye*, 1999].

6.2 Discontinuous intraseasonal EICC

Coastal Ekman pumping by local alongshore wind stress has been shown to be important at seasonal time scales during the peak of the monsoons (in both summer and winter) [*Shankar et al.*, 1996; *McCreary et al.*, 1996]. In order to isolate the intraseasonal component of the alongshore wind, we applied the same filtering procedure (high-pass Hanning filter) as for the altimetric current. The intraseasonal variability is comparable to (indeed, slightly larger than) that of the seasonal cycle (not shown). Given that the annual alongshore wind variability is among the prominent forcing mechanisms of the annual variability of the EICC, we conjecture that the intraseasonal alongshore wind must similarly account for a significant part of the observed intraseasonal EICC variability. The correlation matrix (Table 8) showed significant values only between pairs of neighbouring points, implying that the local forcing of the intraseasonal EICC contributes to its discontinuity from north to south.

Unlike at interannual frequencies (Section 6.1), the effect of interior Ekman pumping in the observed discontinuity cannot be quantified at intraseasonal frequencies using Equation (2) because of the beta-dispersion of Rossby waves [*Schopf et al.*, 1981] that can not be ignored at these frequencies [*J. McCreary*, personal communication]. To account for it requires a numerical model, which is beyond the scope of this paper and will be addressed in a future study.

The role of remote forcing from the eastern boundary of the bay or from the equatorial Indian Ocean can also not be elucidated without a numerical model [*Shankar et al.*, 1996]. Nevertheless, we can make some inferences because our current data set is restricted to the surface of the ocean. The

theory of linear boundary-trapped waves predicts that in a continuously stratified ocean, the propagation of the wave signal is not strictly horizontal: some bending of the coastal Kelvin wave rays and that of Rossby wave rays is expected to take place along the propagation path [e.g. *Romea and Allen*, 1983; *McCreary*, 1984]. Specifically, the ocean physics operates a selection of time scales, the downward slope of the Kelvin and Rossby wave beams scaling as a linear function of the wave frequency. *Nethery and Shankar* [2007] applied an analytical, continuously stratified ocean model to prove that at intraseasonal periods (typically a few months), a surface Kelvin wave signal at the southern tip of Sri Lanka bends significantly downward along its propagation path along the Indian west coast and escapes the surface (typically 0–60 m) layer after travelling over 10° of latitude. It follows that the part of the intraseasonal variability of the surface EICC that is driven remotely by boundary-trapped waves (and by the Rossby waves they could trigger during their propagation along the eastern boundary of the bay) should not be highly correlated along the western boundary of the Bay of Bengal.

The remaining mechanism to be considered is the western boundary turbulence generated by the nonlinearities (typically barotropic and/or baroclinic instabilities). Its role in the observed discontinuity of the EICC is impossible to assess without an eddy-resolving numerical model; it is possible, however, that this mechanism also contributes to decorrelate the EICC variability along its path, given that its spatial scale is much smaller than the dimension of the basin.

7. Summary and discussion

We have used a newly processed altimeter data set to present a hitherto unprecedented description of the spatio-temporal structure of the EICC. The data set resolves time scales ranging from a few months (intraseasonal) to a few years (interannual), and the high along-track resolution yields the first description of the cross-shore structure of the current.

Our analysis confirmed what was known about the seasonal cycle of the EICC from observations (hydrography and ship drifts) and numerical model studies. First, the data showed that the seasonal cycle dominates the variability at all locations. Second, there are two distinct regimes, the EICC being correlated alongshore north of 15°N and south of 10°N, with the two regimes being out of phase [*Eigenheer and Quadfasel*, 2000; *Shankar*, 2000] owing to the sharp change in the Ekman pumping field at 12°N [*Shankar et al*., 1996; *McCreary et al*., 1996]. This conformity with earlier, historical data is to be expected because even the gridded altimeter data sets, though not capable of resolving the cross-shore variability of the EICC [D08], are not at variance with the hydrographic and ship-drift data [see, for example, *Shankar et al.*, 2002]. The length of the time

series, however, permits an extension to the entire 1992–2002 period of what was earlier known from climatologies (like ship drifts) and year-specific observations (like hydrographic data).

Our data set revealed that the typical cross-shore length scale of the EICC increased from 60 km in the northern bay to 150 km south of Sri Lanka. This trapping scale is somewhat greater than but comparable to *Ro*, the *e*-folding scale associated with boundary-trapped waves. While the trapping is evident in hydrographic and ship-drift data, and is simulated by numerical models, our data set is the only one that has high enough resolution to capture the EICC cross-shore structure. The equatorward increase in the trapping scale provides empirical support for the use of linear wave theory in model studies [*Shankar et al.*, 1996; *McCreary et al.*, 1996]. Nevertheless, from this study alone we can not rule out a significant role for nonlinear dynamics. Elucidating the role of nonlinearity, however, calls for a dedicated modeling study, which is beyond the scope of this paper.

The data set also revealed considerable year-to-year modulation of the seasonal cycle. In spite of the annual time scale dominating the spectrum of variability, the EICC presents a wide range of time scales, ranging from two months to a few years. The non-annual time scales globally concentrate as much energy as the annual time scale all along the EICC path. The year-to-year variability is considerable, taking the form of short-lived (typical duration was a few weeks), intense (of order 1 m s^{-1}) bursts. The magnitude of these intraseasonal bursts does not seem to be related to the timing of the seasonal cycle; a similar lack of relation of the intraseasonal bursts to the phase of the seasonal cycle was noted in current-meter data from south of Sri Lanka [*Schott et al.*, 1994].

Unlike the seasonal component of the EICC, however, the interannual and intraseasonal components are decorrelated along the coast. An analytical analysis showed that the decorrelation of the interannual EICC is linked to the Ekman pumping field over the bay; the decorrelation of local alongshore winds contributed to the decorrelation of the intraseasonal EICC. The role of the other known forcing mechanisms of the EICC — remote forcing by winds blowing along the eastern and northern boundaries of the bay and by winds in the equatorial Indian Ocean, and by intraseasonal variability of the interior Ekman pumping [*Shankar et al.*, 1996; *McCreary et al.*, 1996] — need to be investigated with a numerical model. The downward propagation of Kelvin wave beams into the deep ocean at intraseasonal periods [*Nethery and Shankar*, 2007], however, limits the possible impact of the remote processes on the intraseasonal component of the surface EICC described by this data set.

The alongshore decorrelation notwithstanding, the EICC was highly correlated at all time scales in the cross-shore direction. Analysis showed that the EICC is trapped within about one *Ro* of the shelf at all time scales, with the current beyond one *Ro* flowing in the direction opposite to the

EICC at most locations. Together with the alongshore decorrelation of the raw EICC data, this shear implies the existence of recirculating loops (Figure 13).

Thus, the EICC appears globally as an inherently discontinuous flow from the northern bay to the southern tip of Sri Lanka, taking the form of a few recirculating loops along the EICC path, with a typical cross-shore spatial scale of 150–200 km. The loops are highly variable in direction at all time scales from intraseasonal (not shown) to interannual (Figure 14). The timings of the reversals of the various recirculations hugging the western boundary also appeared to be independent of one another.

That the EICC is highly discontinuous in space and time implies that there is no guarantee that the basic pathways and advective time scales of the inter-basin exchange of water masses between the Bay of Bengal and the Arabian Sea, identified in earlier studies using coarse and/or climatological numerical simulations [e.g. *Jensen*, 2001, 2007; *Han et al*., 2001; *Durand et al*, 2007], are robust when the full spatio-temporal range of variability of the EICC and associated recirculations is resolved. Yet, the data did confirm that the time window of possible export of low-salinity Bay-of-Bengal water to the Arabian Sea via the western boundary of the bay is almost limited to the period November–December [*Schott et al*., 1994].

Finally, the observations reported in the present paper set some stringent dimensioning constraints in space and time for in situ observing systems as well as for numerical models of the EICC. In order to observe or model its full range of variability, it appears necessary to resolve at least one *Ro* (from the shelf) and a few weeks all along its path from the northern bay to the southern tip of Sri Lanka.

Acknowledgements. This study was funded by IRD, LEGOS and NIO. Support from these institutions is gratefully acknowledged. DS and SSCS thank CSIR and INCOIS/MoES, India for financial support. We are indebted to the scientists involved in the MAP project for working out the raw SLA processing algorithm. We thank Julian McCreary for sharing his insights into the dynamics of the north Indian Ocean. We also thank him and an anonymous reviewer for having done a very useful review, which helped considerably to improve the quality of our manuscript. We made extensive use of the SAXO software (http://forge.ipsl.jussieu.fr/saxo) developed by Sébastien Masson for plotting. This is NIO contribution 4484.

REFERENCES

AVISO (1996), AVISO user handbook: Merged TOPEX/Poseidon products, *Tech. Rep. AVI-NT-02-101-CN*, ed. 3.0, 198pp, Toulouse, France.

Babu, M. T., Y. V. B. Sarma, V. S. N. Murty, and P. Vethamony (2003), On the circulation in the Bay of Bengal during Northern spring inter-monsoon (March April 1987), *Deep-Sea Res. II(50)*, 855–865.

Bentamy, A., Y. Quilfen, F. Gohin, N. Grima, M. Lenaour, and J. Servain (1996), Determination and validation of average wind fields from ERS-1 scatterometer measurements, *Global Atmos. Ocean Syst., 4,* 1–29.

Birol, F., L. Roblou, F. Lyard, W. Llovel, F. Durand, L. Renault, B. Dewitte, R. Morrow, and Y. Ménard (2006), Towards using satellite altimetry for the observation of coastal dynamics. Symposium "15 Years of Progress in Radar Altimetry", Venice, Italy. http://earth.esa.int/workshops/venice06/participants/855/paper_855_birol.pdf.

Carrère, L., and F. Lyard (2003), Modeling the barotropic response of the global ocean to atmospheric wind and pressure forcing-Comparisons with observations, *Geophys. Res. Lett.*, *30*, 1275, doi:10.1029/2002GL016473).

Chelton, D. B., R. A. deSzoeke, M. G. Schlax, K. El Naggar, and N. Siwertz (1998), Geographical variability of the first baroclinic Rossby radius of deformation, *J. Phys. Oceanogr., 28*, 433–460.

Clarke, A. J. (1977), Wind-forced linear and nonlinear Kelvin waves along an irregular coastline, *J. Fluid Mech., 83*, 337–348.

Clarke, A. J., and X. Liu (1994), inter-annual Sea Level in the Northern and Eastern Indian Ocean, *J. Phys. Oceanogr*., *24*, 1224–1235.

Cutler, A. N., and J. C. Swallow (1984), Surface currents of the Indian Ocean (to 25°S, 100°E): Compiled from historical data archived by the Meteorological Office, Bracknell, UK, Report 187, 36charts, 8pp, Institute of Oceanographic Sciences, Wormley, England.

Durand, F., D. Shankar, C. de Boyer Montégut, S. S. C. Shenoi, B. Blanke, and G. Madec (2007), Modeling the barrier-layer formation in the South-Eastern Arabian Sea, *J. Clim., 20*, 10, 2109–2120.

Durand, F. D. Shankar, F. Birol, and S.S.C. Shenoi (2008), Estimating boundary currents from satellite altimetry: A case study for the east coast of India. *J. Oceanogr.*, *64,* 831–845.

Eigenheer, A., and D. Quadfasel (2000), Seasonal variability of the Bay of Bengal circulation inferred from TOPEX/Poseidon altimetry, *J. Geophys. Res., 105*, 3243–3252.

Gill, A. E. (1982), *Atmosphere-Ocean Dynamics*, Academic Press, London, UK.

Godfrey, J. S. (1975), On ocean spindown I: A linear experiment, *J. Phys. Oceanogr., 5*, 399–409.

Han, W., J.P. McCreary, and K. Kohler (2001), Influence of precipitation minus evaporation and Bay of Bengal rivers on dynamics, thermodynamics, and mixed-layer physics in the upper Indian Ocean, *J. Geophys. Res., 106*, 6895–6916.

Han, W., and P. Webster (2002), Forcing Mechanisms of Sea Level inter-annual Variability in the Bay of Bengal, *J. Phys. Oceanogr., 32*, 216–239.

Jensen, T. G. (2001), Arabian Sea and Bay of Bengal exchange of salt and tracers in an ocean model, *Geophys. Res. Lett., 28*, 3967–3970.

Jensen, T. G. (2007), Wind-Driven Response of the Northern Indian Ocean to Climate Extremes, *J. Clim., 20*, 2978–2993, doi:10.1175/JCLI4150.1.

Kessler, W. S., and L. Gourdeau (2007), The annual cycle of circulation of the southwest subtropical Pacific analyzed in an ocean GCM, *J. Phys. Oceanogr., 37*, 1610–1627.

Levitus, S., and T. P. Boyer (1994), *World Ocean Atlas 1994*, vol. 4, *Temperature*, *NOAA Atlas NESDIS 4*, 117 pp.

Levitus, S., R. Burgett, and T. P. Boyer (1994), *World Ocean Atlas 1994*, vol. 3, *Salinity*, *NOAA Atlas NESDIS 3*, 99 pp.

Lyard, F., F. Lefevre, T. Letellier, and O. Francis (2006), Modelling the global ocean tides: modern insights from FES2004, *Ocean Dynamics, 56*, 394–415.

McCreary, J. P. (1984), Equatorial beams, *J. Mar. Res., 42*, 395–430.

McCreary, J. P., P. K. Kundu, and R. L. Molinari (1993), A numerical investigation of the dynamics, thermodynamics and mixed-layer processes in the Indian Ocean, *Prog. Oceanogr., 31*, 181–244.

McCreary, J. P., W. Han, D. Shankar, and S. R. Shetye (1996), Dynamics of the East India Coastal Current, 2. Numerical solutions, *J. Geophys. Res., 101*, 13,993–14,010.

Mariano, A. J., E. H. Ryan, B. D. Perkins, and S. Smithers (1995), The Mariano Global Surface Velocity Analysis 1.0,USCG Report CG-D-34-95, 55 pp.

Murtugudde, R., B. Goswami, and A. J. Busalacchi (1998), Air-sea interaction in the southern tropical Indian Ocean and its relation to interannual variability of the monsoon over India. In: Proceedings of International Conference on Monsoon and Hydrological Cycle, Kyongju, Korea, 22–25 April 1998, pp. 184–88.

Murtugudde, R., J. P. McCreary, and A. J. Busalacchi (2000), Oceanic processes associated with anomalous events in the Indian Ocean with relevance to 1997–1998, *J. Geophys. Res., 105*, 3295–3306.

Nethery, D., and D. Shankar (2007), Vertical propagation of baroclinic Kelvin waves along the west coast of India, *J. Earth Syst. Sci., 116*, 331–339.

Potemra, J. T., M. E. Luther, and J. J. O'Brien (1991), The seasonal circulation of the upper ocean in the Bay of Bengal, *J. Geophys. Res., 96*, 12,667–12,683.

Press, W. H., S. A. Teukolsky, W. T. Vetterling, and B. P. Flannery (1992), *Numerical Recipes in Fortran 77, The Art of Scientific Computing*, 935pp., Cambridge University Press.

Rao, S., S. K. Behera, Y. Masumoto, and T. Yamagata (2002), inter-annual subsurface variability in the Tropical Indian Ocean with a special emphasis on the Indian Ocean Dipole, *Deep-Sea Res. II, 49*, 1549–1572.

Reverdin, G., D. L. Cadet, and D. Gutzler (1986), inter-annual displacement of convection and surface circulation over the equatorial Indian Ocean, *Quart. J. Roy. Met. Soc., 112*, 43–67.

Romea, R. D., and J. S. Allen (1983), On vertically propagating coastal Kelvin waves at low latitudes, *J. Phys. Oceanogr. 13*, 1,241–1,254.

Saji, N. H., B. N. Goswami, P. N. Vinayachandran, and T. Yamagata (1999), A dipole mode in the tropical Indian Ocean, *Nature, 401*, 360–363.

Sanilkumar, K. V., T. V. Kuruvilla, D. Jogendranath, and R. R. Rao (1997), Observations of the Western Boundary Current of the Bay of Bengal from a hydrographic survey during March 1993*, Deep Sea Res. I, 44*, 1, 135–145.

Schopf, P. F., D. L. T. Anderson, and R. Smith (1981), Beta-dispersion of low-frequency Rossby waves, *Dyn. Atmosph. Oc., 5*, 187–214.

Schott, F., J. Reppin, J. Fischer, and D. Quadfasel (1994), Currents and transports of the Monsoon Current south of Sri Lanka, *J. Geophys. Res., 99*, 25,127–25,142.

Schott, F., and J. P. McCreary (2001), The monsoon circulation in the Indian Ocean, *Progr. Oceanogr., 51*, 1–123.

Shankar, D., J. P. McCreary, W. Han, and S. R. Shetye (1996), On the dynamics of the East India Coastal Current, part 1, Analytic solutions forced by interior Ekman pumping and local alongshore winds, *J. Geophys. Res., 101*, 13975–13991.

Shankar, D. (1998), Low-frequency variability of sea level along the coast of India, Ph.D. thesis, Goa University, India.

Shankar, D. (2000), Seasonal cycle of sea level and currents along the coast of India, *Curr. Sci., 78*, 279–288.

Shankar, D., and S. R. Shetye (1999), Are interdecadal sea level changes along the Indian coast influenced by variability of monsoon rainfall? *J. Geophys. Res., 104*, 26031–26042.

Shankar, D., and S. R. Shetye (2001) Why is mean sea level along the coast of India higher in the Bay of Bengal than in the Arabian Sea? *Geophys. Res. Lett*., 28, 563–565.

Shankar, D., P. N. Vinayachandran, and A. S. Unnikrishnan (2002), The monsoon currents in the north Indian Ocean, *Progr. Oceanogr., 52*, 63–120.

Shenoi, S. S. C., D. Shankar, and S. R. Shetye (1999a), On the sea surface temperature high in the Lakshadweep Sea before the onset of the southwest monsoon, *J. Geophys. Res., 104*, 15,703–15,712.

Shenoi, S. S. C., P. K. Saji, and A. M. Almeida (1999b), Near-surface circulation and kinetic energy in the tropical Indian Ocean derived from Lagrangian drifters, *J. Mar. Res., 57*, 885–907.

Shetye, S. R., S. S. C. Shenoi, A. D. Gouveia, G. S. Michael, D. Sundar, and G. Nampoothiri (1991), Wind-driven coastal upwelling along the western boundary of Bay of Bengal during southwest monsoon, *Cont. Shelf Res., 11*, 1397–1408.

Shetye, S. R., A. D. Gouveia, S. S. C. Shenoi, D. Sundar, G. S. Michael, and G. Nampoothiri (1993), The western boundary current of the seasonal subtropical gyre in the Bay of Bengal, *J. Geophys. Res., 98*, 945–954.

Shetye, S. R., A. D. Gouveia, D. Shankar, S. S. C. Shenoi, P. N. Vinayachandran, D. Sundar, G. S. Michael, and G. Nampoothiri (1996), Hydrography and circulation in the western Bay of Bengal during the northeast monsoon, *J. Geophys. Res., 101*, 14,011–14,025.

Sindhu, B. I. Suresh, A. S. Unnikrishnan, N. V. Bhatkar, S. Neetu, and G. S. Michael (2007), Improved bathymetric data sets for the shallow water regions in the Indian Ocean, *J. Earth Syst. Sci.*, 116, 261–274.

Srinivas, K., P. K. D. Kumar, and C. Revichandran (2005), ENSO signature in the sea level along the coastline of the Indian subcontinent, *Ind. J. Mar. Sci.*, *34*, 225–236.

Thompson, B., C. Gnanaseelan, and P. S., Salvekar (2006), Variability in the Indian Ocean circulation and salinity and its impact on SST anomalies during dipole events, *J. Mar. Res., 64*, 853–880.

Toumazou, V., and J.-F. Cretaux (2001), Using a Lanczos Eigensolver in the Computation of Empirical Orthogonal Functions, *Mon. Wea. Rev., 129*,1243–1250.

Vignudelli S., P. Cipollini, M. Astraldi, G. P. Gasparini, and G. M. R. Manzella (2000), Integrated use of altimeter and in situ data for understanding the water exchanges between the Tyrrhenian and ligurian seas, *J. Geophys. Res*., *105*, 19649–19663.

Vinayachandran, P. N., S. R. Shetye, D. Sengupta, and S. Gadgil (1996), Forcing mechanisms of the Bay of Bengal circulation, *Curr. Sci., 71*, 753–763.

Vinayachandran, P. N., T. Kagimoto, Y. Masumoto, P. Chauhan, S. R. Nayak, and T. Yamagata (2005), Bifurcation of the East India Coastal Current east of Sri Lanka, *Geophys. Res. Lett*., *32*, L15606, doi10.1029/2005GL022864.

Vinayachandran, P. N., D. Shankar, J. Kurian, F. Durand, and S. S. C. Shenoi (2007), Arabian Sea Mini Warm Pool and the Monsoon Onset Vortex*, Curr. Sci., 93*, 203–214.

Webster, P. J., A. M. Moore, J. P. Loschnigg, and R. R. Leben (1999), Coupled ocean-atmosphere dynamics in the Indian Ocean during 1997–1998, *Nature, 401*, 356–360.

Yu, L., J. J. O'Brien, and J. Yang (1991), On the remote forcing of the circulation in the Bay of Bengal, *J. Geophys. Res., 96*, 20,449–20,454.

Tables

	A	B	C	D	E	F	G
Longitude (°E)	87.8	85.7	83.5	81.3	80.8	82.1	79.7
Latitude (°N)	20.8	19.0	17.4	15.8	9.9	6.2	4.9
Distance to the nearest shore (km)	84.4	71.9	45.7	35.8	60.7	54.9	134.7
Bathymetry (m)	63	1199	615	288	289	4252	4202

Table 1. Positions of the EICC points discussed in the paper.

Reference point	A	B	C	D	E	F
B	**0.32** (141)					
C	**0.26** (131)	**0.30** (195)				
D	0.16 (64)	0.20 (56)	**0.27** (91)			
E	0.13 (100)	0.23 (84)	**0.30** (146)	**0.42** (75)		
F	-0.07 (126)	**-0.26** (101)	0.13 (178)	0.21 (93)	**0.29** (142)	
G	-0.36 (49)	-0.20 (45)	-0.01 (82)	**0.44** (40)	**0.33** (64)	**0.49** (77)

Table 2. Correlation matrix of the EICC speed anomaly between the EICC points. Indicated between brackets are the number of data in the time series available to compute the correlation coefficient. The correlation values that exceed the 95% significance level are in bold.

Track #	14	192	116	40	155	218
e-folding scale (km)	23	60	57	27	67	178
Ro/2 (km)	25	30	35	35	50	95

Table 3. The *e*-folding scale of the annual power of the cross-track current, along with the value of *Ro*/2 (based on *Chelton et al.* [1998]) expected from the linear theory.

Reference point	A	B	C	D	E	F
B	**0.62**					
C	**0.70**	**0.60**				
D	0.30	-0.07	**0.30**			
E	-0.03	-0.21	**0.31**	**0.68**		
F	**-0.40**	**-0.60**	-0.09	**0.37**	**0.66**	
G	**-0.39**	**-0.41**	-0.11	**0.43**	**0.55**	**0.82**

Table 4. Correlation matrix of the annual component of EICC speed anomaly between the various points. The correlation values that exceed the 95% significance level are in bold.

Reference point	A	B	C	D	E	F
B	**0.39**					
C	**0.22**	**0.19**				
D	**0.40**	-0.26	0.13			
E	0.16	**0.30**	**0.41**	0.20		
F	-0.22	-0.02	**0.31**	0.15	**0.50**	
G	-0.09	-0.18	-0.15	0.15	0.08	**0.35**

Table 5. Same as Table 4, but for the interannual component of the time series.

Reference point	A	B	C	D	E	F
B	0.19					
C	0.08	0.14				
D	0.06	0.03	0.14			
E	-0.02	0.18	0.15	0.09		
F	-0.02	0.04	0.19	0.09	0.01	
G	-0.11	0.13	0.04	0.08	0.22	0.18

Table 6. Same as Table 4, but for the intraseasonal component of the time series.

Reference point	B	C	D	E
C	**-0.43**			
D	0.11	-0.15		
E	**0.39**	0.09	0.32	
F	-0.07	-0.01	0.20	0.10

Table 7. Same as Table 4, but for the interannual component of the western boundary transport driven by the Rossby wave model.

Reference point	A	B	C	D	E	F
B	**0.73**					
C	**0.53**	**0.84**				
D	**0.36**	**0.66**	**0.84**			
E	0.25	0.31	0.29	**0.33**		
F	0.21	**0.38**	**0.46**	**0.54**	**0.70**	
G	-0.22	-0.18	-0.11	0.0	0.05	0.28

Table 8 Same as Table 4, but for the intraseasonal component of the alongshore wind stress.

Figure captions

Figure 1. (Top) The region of interest (north Indian Ocean) and the regime of the EICC. The thick lines show the axis along which the ship drifts (see Figure 2) are extracted and projected. (Bottom) Layout of the T/P altimetric tracks portions used in the study (thick grey lines). Each T/P track number is indicated in black squares. The position of the reference point of each track (A, B, C, D, E, F, G) used subsequently in the paper is marked with a black star. The 200 m, 1000 m, 2000 m and 3000 m isobaths are shown. Bathymetry is from *Sindhu et al*. [2007].

Figure 2. Seasonal climatology of EICC surface velocity as a function of latitude along Sri Lankan (6°N to 8°N) and Indian (10°N to 21°N) east coasts, inferred from *Mariano et al.* [1995] ship drifts projected in the alongshore direction. Contour interval is 0.2 m s^{-1}. Positive values indicate eastward and northward current. Negative values are shaded.

Figure 3. Data coverage of the cross-track geostrophic surface current anomaly for each track. It is plotted as a function of time (from November 1992 to July 2002). One thin vertical solid (dashed) line is drawn every 1 January (1 July). The position of each point along the track is defined as the distance (in km) from the point to the nearest shore (except for Track #142 located west of Sri Lanka, where it is plotted as a function of latitude). Superimposed (horizontal dotted lines) are the positions of the reference points (A to G; see Figure 1) along the tracks.

Figure 4. Evolution, during 1992–2002, of the raw (unfiltered) altimetric cross-track geostrophic current anomaly for points A (panel a) to G (panel g) (dots). Superimposed on the raw current is the corresponding seasonal climatology (solid line) of the current anomaly (computed as a simple monthly average of the raw current time series). All currents are positive poleward (points A to F) and eastward (point G).

Figure 5. Lomb periodograms of the cross-track geostrophic surface current anomaly for each EICC point. The 95% significance level is indicated by dashed lines.

Figure 6. Seasonal climatology of surface current at the EICC points A to G (see map in Figure 1). The thick lines represent the *Mariano et al.* [1995] ship drifts projected in the alongshore direction, the thin dashed lines the altimetric cross-track geostrophic current anomaly we retrieved, and the thin solid lines the sum of altimetric cross-track geostrophic current anomaly and Ekman drift (estimated from ERS, the European Remote Sensing Satellite: *Bentamy et al.* [1996]) scatterometer, and projected in the cross-track direction). The grey shading is the interannual envelope of the total (geostrophic plus Ekman) current. All currents are positive poleward (points A to F) and eastward (point G). On each panel, we indicate the percentage of the total variance of the geostrophic current explained by the seasonal climatology.

Figure 7. Non-normalized Lomb periodograms of the annual variability of cross-track geostrophic current for all the tracks. The power of the annual component of the cross-track current is plotted as a function of the position along the altimetric track (panels a to f) and as a function of latitude (panel g). Only the values exceeding the 95% significance levels are plotted. Below each periodogram, we present the bathymetry along the track (in m). Superimposed in dotted line are the positions of the reference points (A to G) along the tracks.

Figure 8. (Left) Evolution, during 1993–2001, of the interannual component of the altimetric cross-track geostrophic current anomaly for EICC points A (panel a) to G (panel g). All currents are positive poleward (points A to F) and eastward (point G). The dotted portions show the gappy parts of the original (raw) time series. (Right) Snapshots of the interannual EICC on 1 August 1996 (top) and on 1 May 1997 (bottom). The scale of the current vectors is indicated on the charts.

Figure 9. Evolution, from January to December 1999, of the intraseasonal component of the altimetric cross-track geostrophic current anomaly (thick line) for EICC points A (panel a) to G (panel g). The dotted portions show the gappy parts of the original (raw) time series. Superimposed (thin line) is the corresponding seasonal climatology. All currents are positive poleward (points A to F) and eastward (point G).

Figure 10. Evolution, during 1992–2002, of the anomaly (with respect to the monthly climatology presented in Figure 6) of the altimetric cross-track geostrophic current anomaly (thick line) for EICC points A (panel a) to G (panel g). All currents are positive poleward (points A to F) and eastward (point G). Superimposed (thin line) is the Dipole Mode Index time series (as defined by *Saji et al.* [1999]).

Figure 11. Correlation along each altimetric track of the cross-track geostrophic current anomaly with the reference point (A to G). The positions of the reference points are indicated by dotted lines and the 95% significance level by dashed lines. The decorrelation scale, (defined as the distance between the reference point and the first crossing of the 95% significance level), is indicated on each panel, as is the value of *Ro* from *Chelton et al.* [1998] (in km).

Figure 12. Spatial (top) and temporal (bottom) component of the first EOF mode of the cross-track geostrophic current anomaly, for each altimetric track. The percentage of variance explained by this mode is indicated at the top of each panel. The spatial component is plotted as a function of the position along the altimetric track (panels a to f) and as a function of latitude (panel g). Superimposed in dotted line are the positions of the reference points (A to G) along the tracks. All currents are positive poleward (panels a to f) and eastward (panel g).

Figure 13. Schematic of the EICC circulation pathways. The recirculation cells are represented with arbitrary directions, but with dimensions scaling like the anti-correlation length scales given by Figure 11.

Figure 14. Low-passed (interannual) SLA for the Bay of Bengal from *AVISO* [1996], plotted for some days from 1 July 1994 to 1 July 1999. The date is indicated on each frame. Contour interval is 2 cm.

Figure S1. Spatial component of the first EOF mode of the cross-track geostrophic current anomaly, for each altimetric track. First column concerns the intraseasonal EICC, second column the annual EICC, and third column the interannual EICC. The percentage of variance explained by this mode is indicated at the top of each panel. The spatial component is plotted as a function of the position along the altimetric track (Tracks #14, 192, 116, 40, 155, 218) and as a function of latitude (Track #142). All currents are positive poleward (panels a to f) and eastward (panel g).

Figure S2. Anomaly (with respect to the long-term mean) of the interannual (500 day-low-passed) Ekman pumping velocity (positive upward) in the Bay of Bengal (in m d^{-1}), for six selected dates. The dates correspond to the (positive and negative) relative extrema of the field in the southwestern corner off the basin, east of Sri Lanka, where the maximal variability is found.

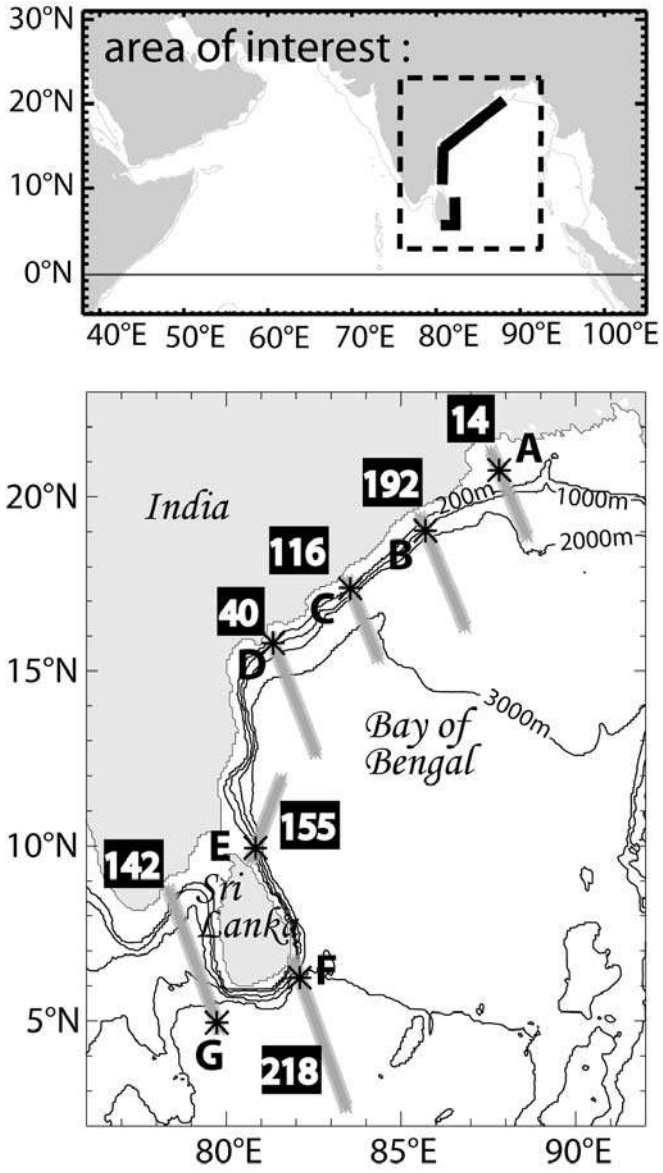
area of interest :
30°N
20°N
10°N
0°N
40°E
50°E
60°E
70°E
80°E
90°E
100°E
India
Bay of Bengal
Sri Lanka
200m
1000m
2000m
3000m
14
192
116
40
155
142
218
A
B
C
D
E
F
G
20°N
15°N
10°N
5°N
80°E
85°E
90°E

Fig.1

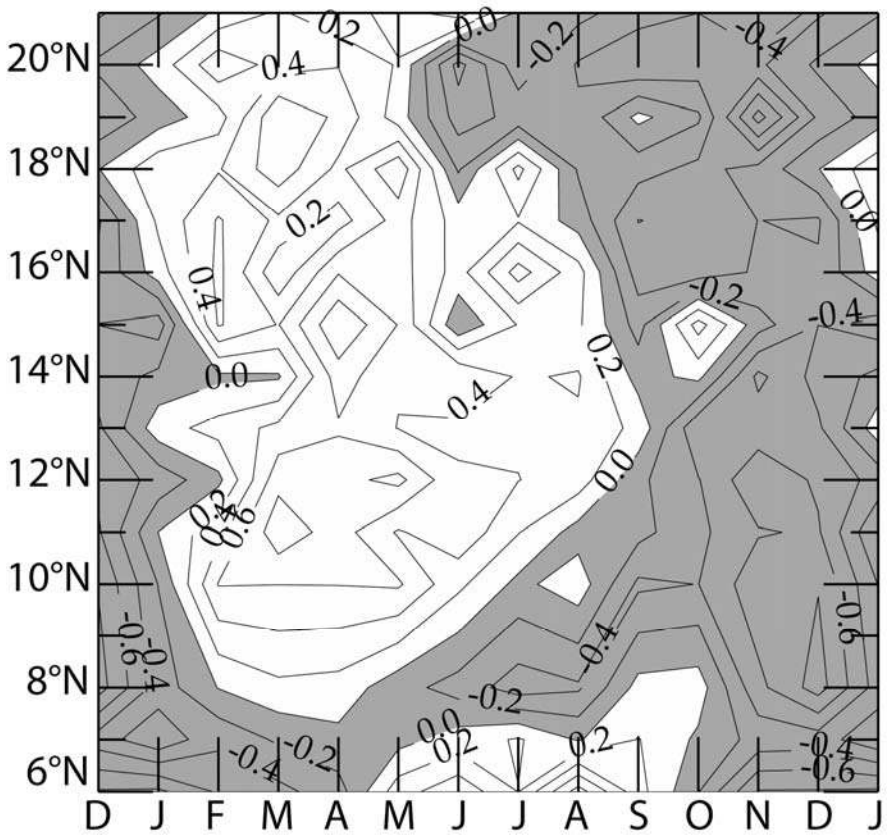

Fig.2

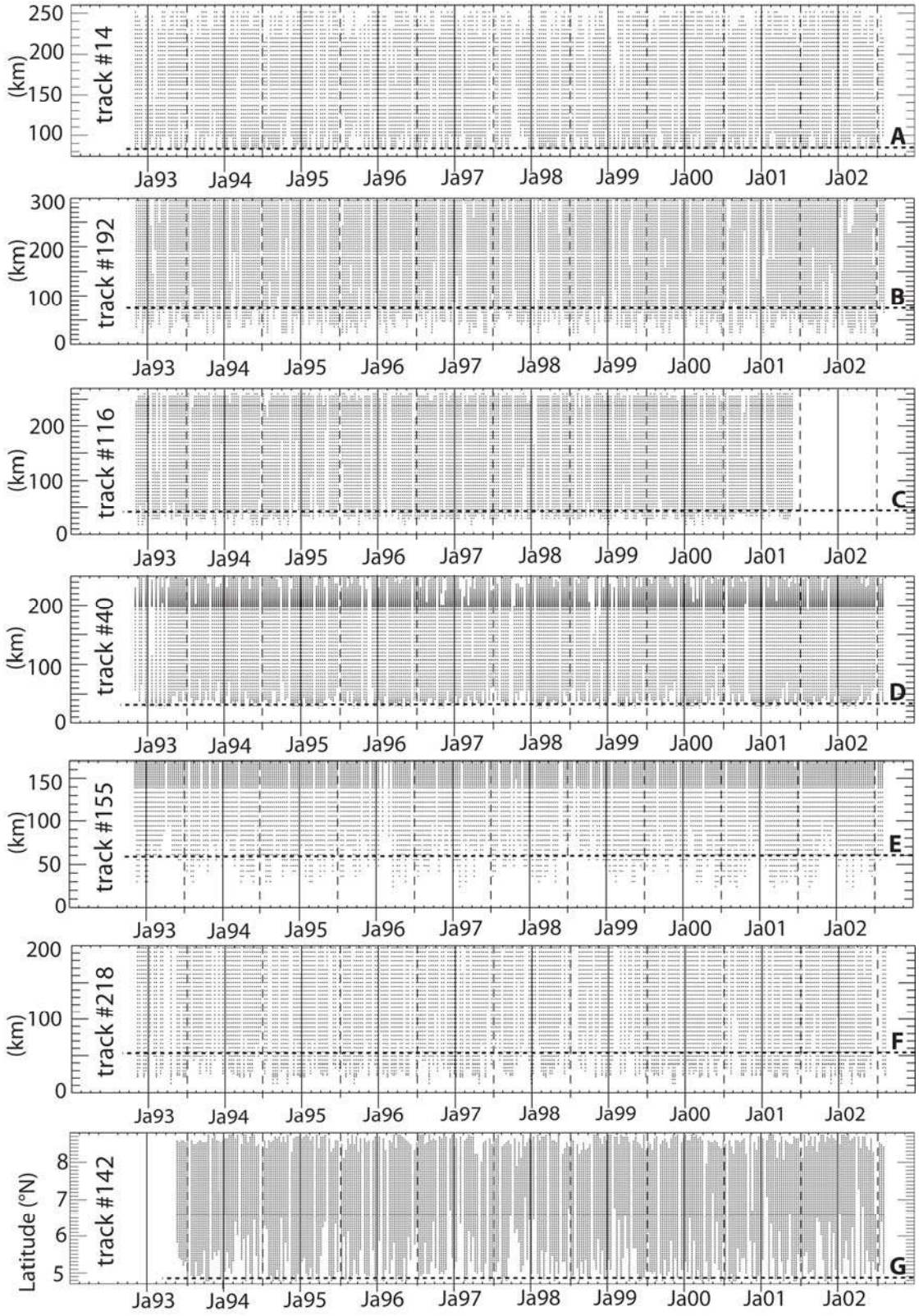
track #14
(km)
250
200
150
100
A
track #192
300
200
100
0
B
track #116
200
100
0
C
track #40
200
100
0
D
track #155
150
100
50
0
E
track #218
200
100
0
F
track #142
Latitude (°N)
8
7
6
5
G
Ja93
Ja94
Ja95
Ja96
Ja97
Ja98
Ja99
Ja00
Ja01
Ja02

Fig.3

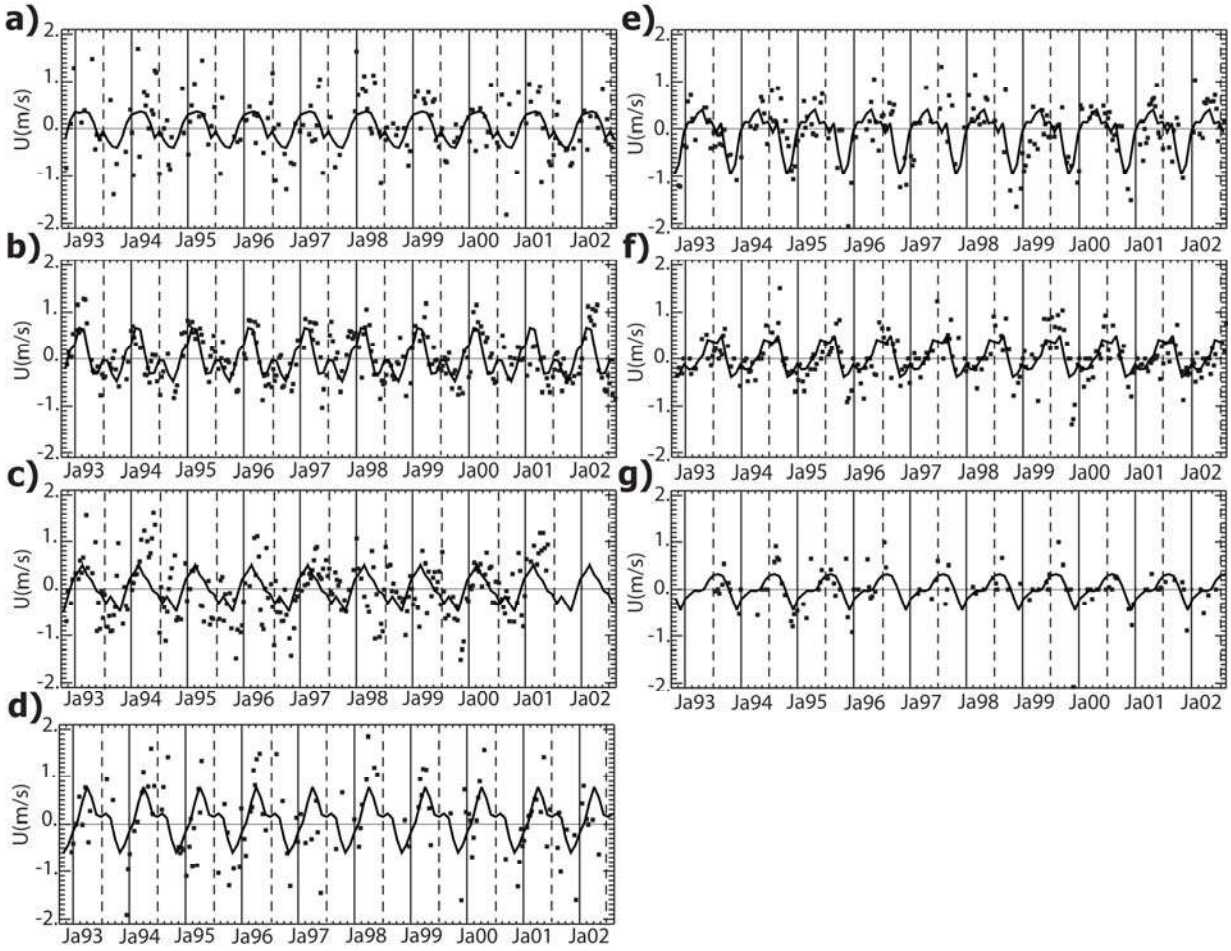
a)
b)
c)
d)
e)
f)
g)
U(m/s)
2.
1.
0.
-1.
-2.
Ja93
Ja94
Ja95
Ja96
Ja97
Ja98
Ja99
Ja00
Ja01
Ja02

Fig.4

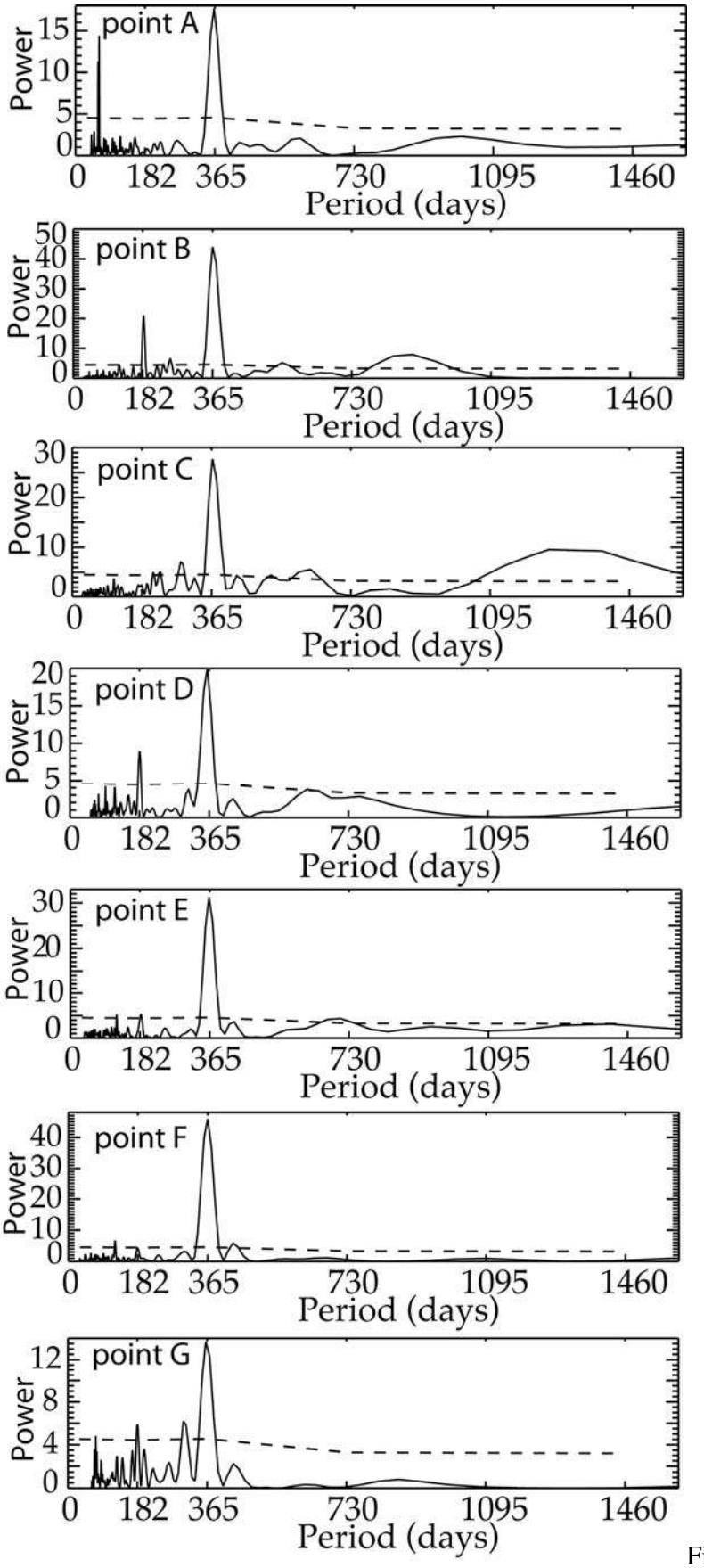
point A
Power
15
10
5
0
0 182 365 730 1095 1460
Period (days)
point B
Power
50
40
30
20
10
0
0 182 365 730 1095 1460
Period (days)
point C
Power
30
20
10
0
0 182 365 730 1095 1460
Period (days)
point D
Power
20
15
10
5
0
0 182 365 730 1095 1460
Period (days)
point E
Power
30
20
10
0
0 182 365 730 1095 1460
Period (days)
point F
Power
40
30
20
10
0
0 182 365 730 1095 1460
Period (days)
point G
Power
12
8
4
0
0 182 365 730 1095 1460
Period (days)

Fig.5

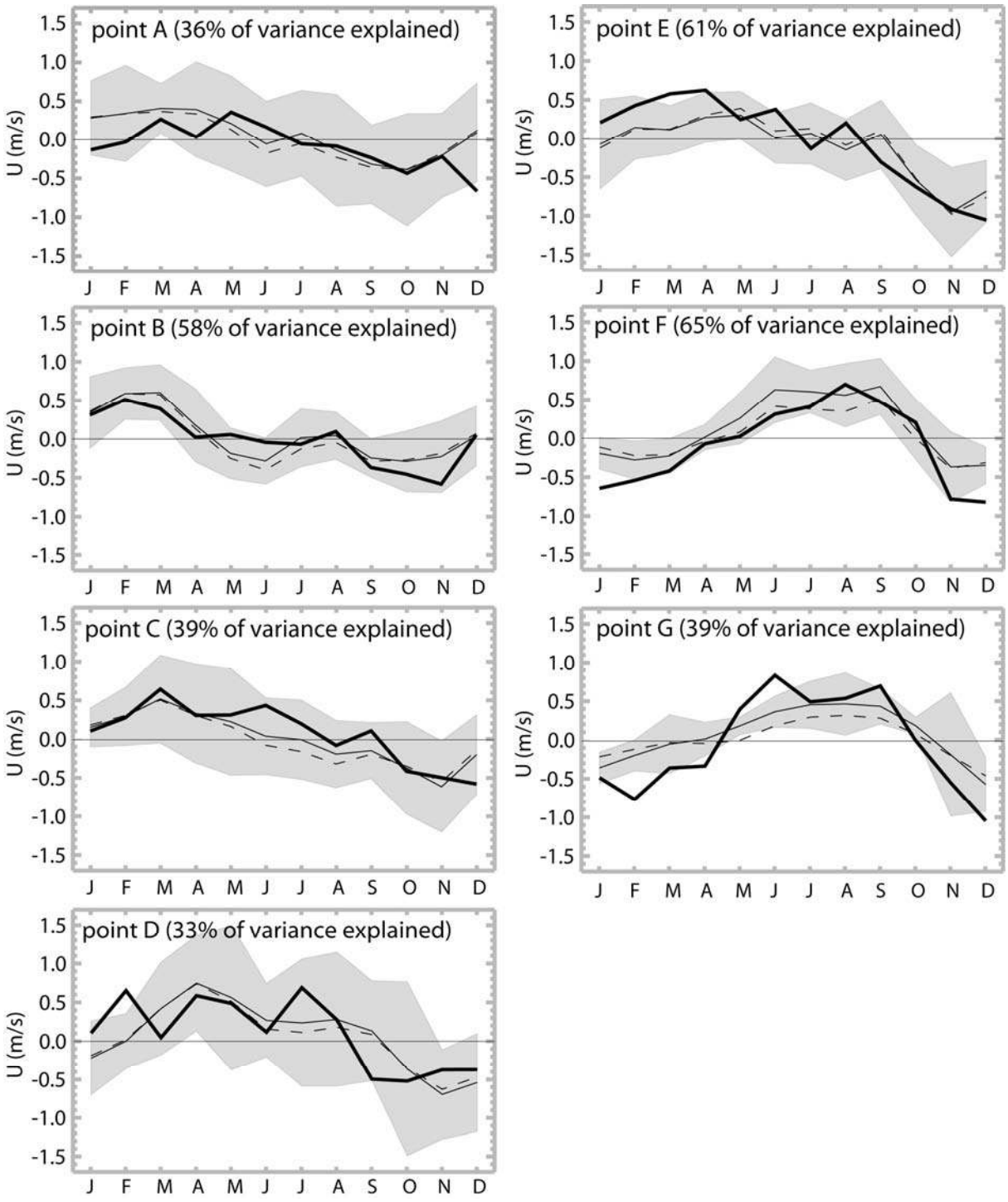
point A (36% of variance explained)
point E (61% of variance explained)
point B (58% of variance explained)
point F (65% of variance explained)
point C (39% of variance explained)
point G (39% of variance explained)
point D (33% of variance explained)
U (m/s)
1.5
1.0
0.5
0.0
-0.5
-1.0
-1.5
J F M A M J J A S O N D

Fig.6

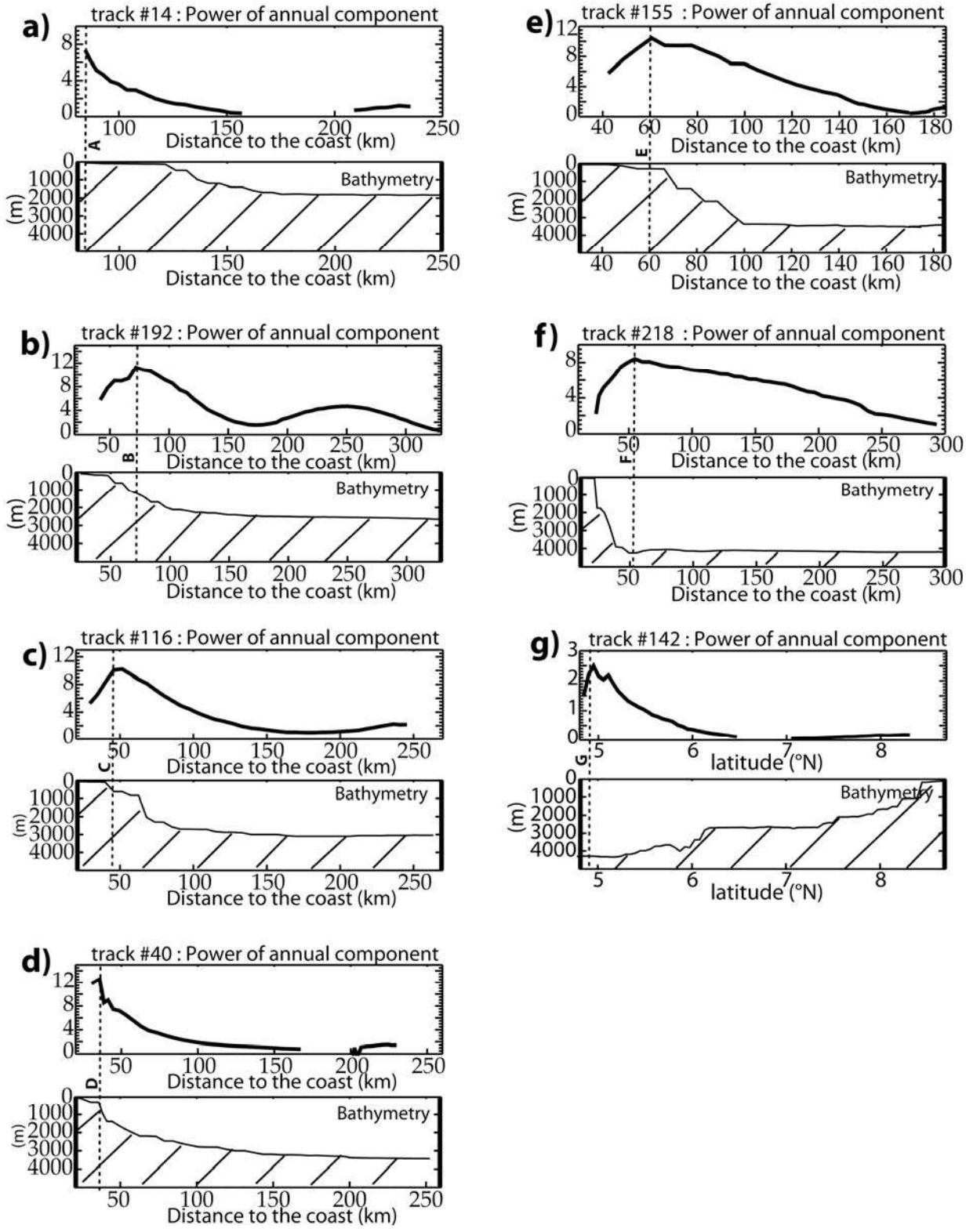
a)
track #14 : Power of annual component
Distance to the coast (km)
A
Bathymetry
(m)
b)
track #192 : Power of annual component
B
c)
track #116 : Power of annual component
C
d)
track #40 : Power of annual component
D
e)
track #155 : Power of annual component
E
f)
track #218 : Power of annual component
F
g)
track #142 : Power of annual component
latitude (°N)
G

Fig.7

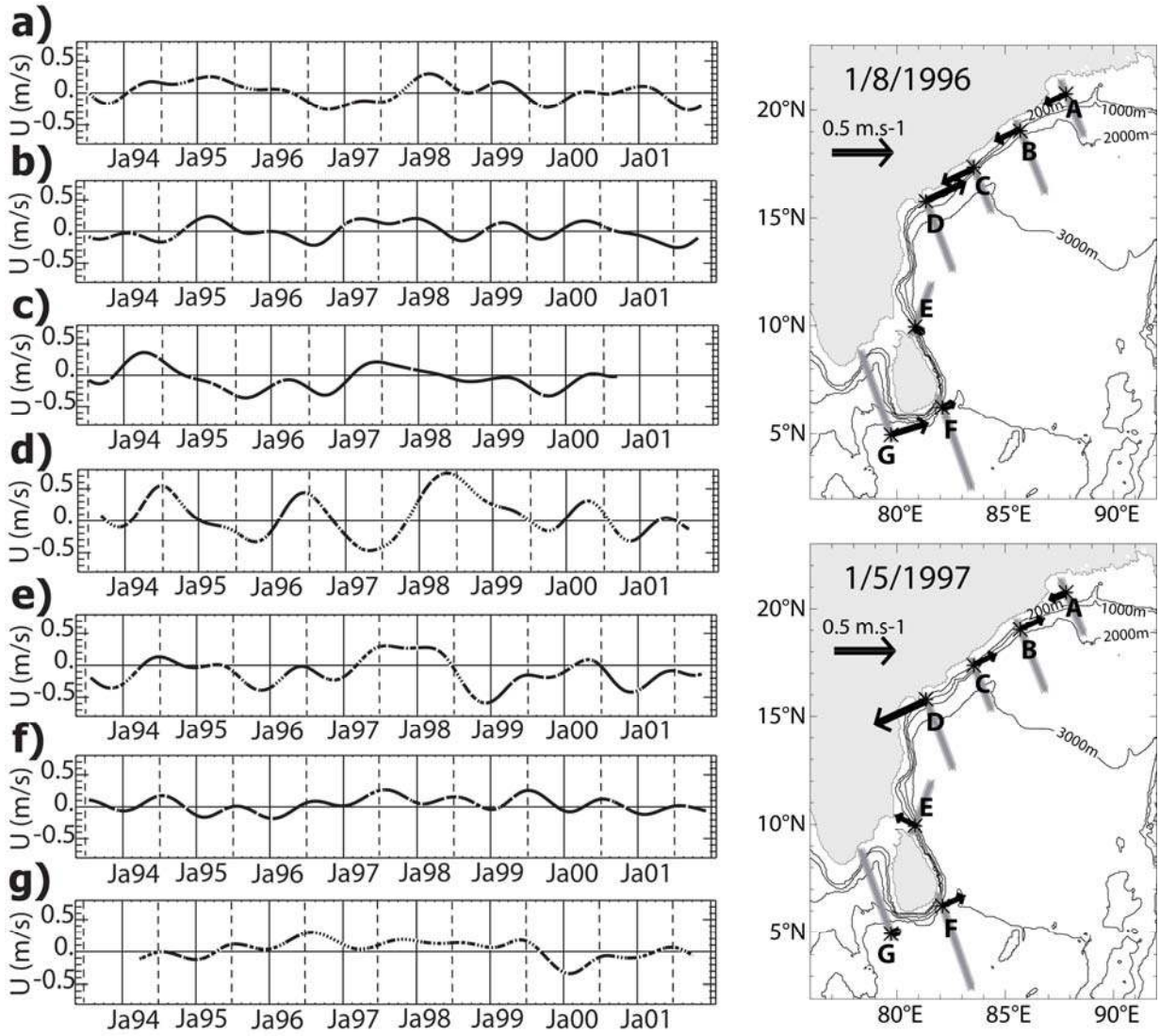
a)
b)
c)
d)
e)
f)
g)
U (m/s)
0.5
0.
-0.5
Ja94 Ja95 Ja96 Ja97 Ja98 Ja99 Ja00 Ja01
1/8/1996
0.5 m.s-1
1/5/1997
0.5 m.s-1
20°N
15°N
10°N
5°N
80°E
85°E
90°E
200m
1000m
2000m
3000m
A
B
C
D
E
F
G

Fig.8

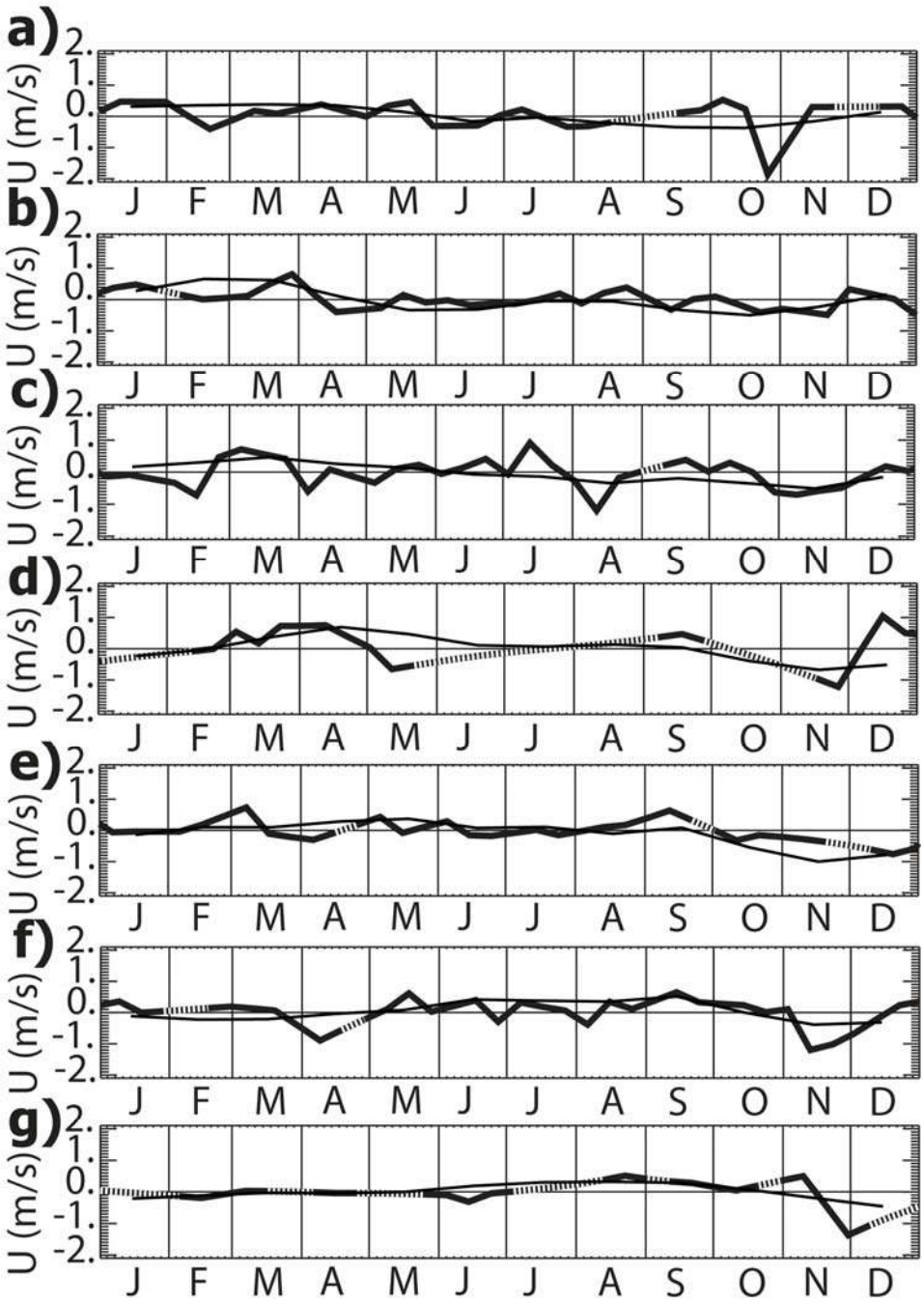

Fig.9

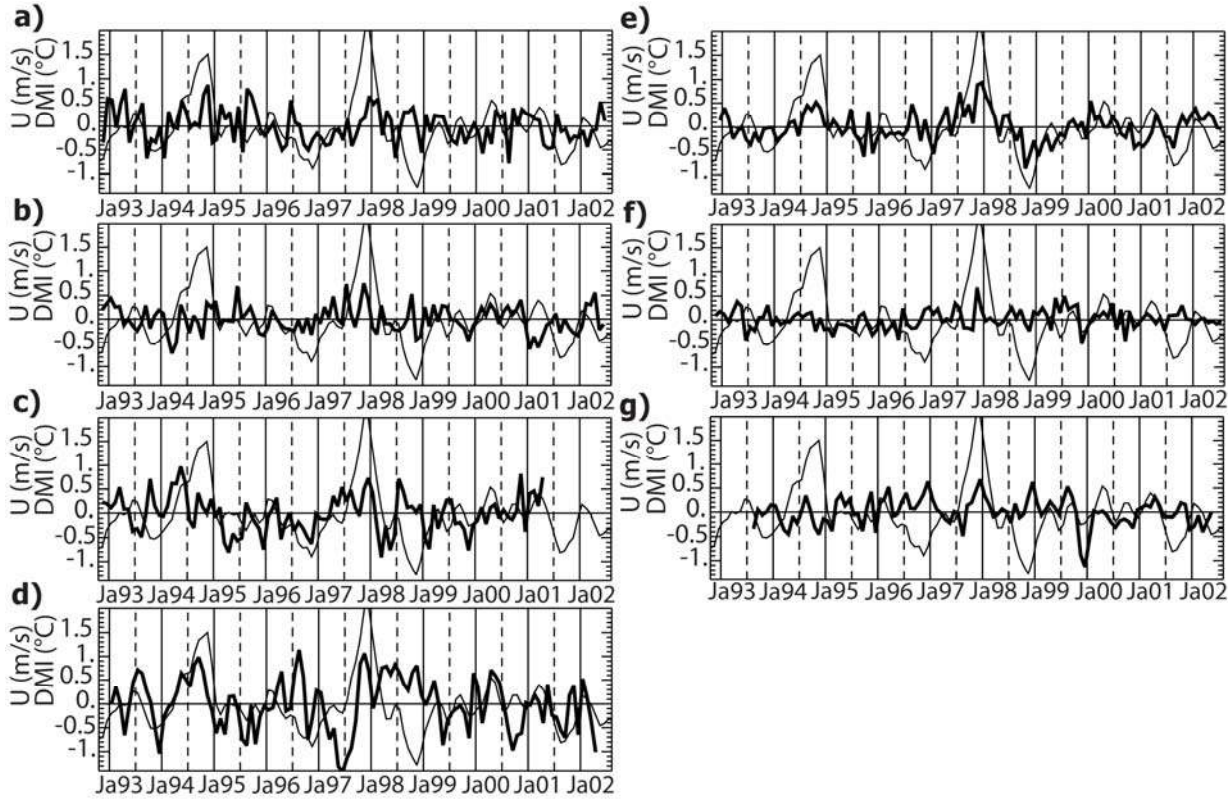
a)
b)
c)
d)
e)
f)
g)
U (m/s)
DMI (°C)
1.5
1.
0.5
0.
-0.5
-1.
Ja93 Ja94 Ja95 Ja96 Ja97 Ja98 Ja99 Ja00 Ja01 Ja02

Fig.10

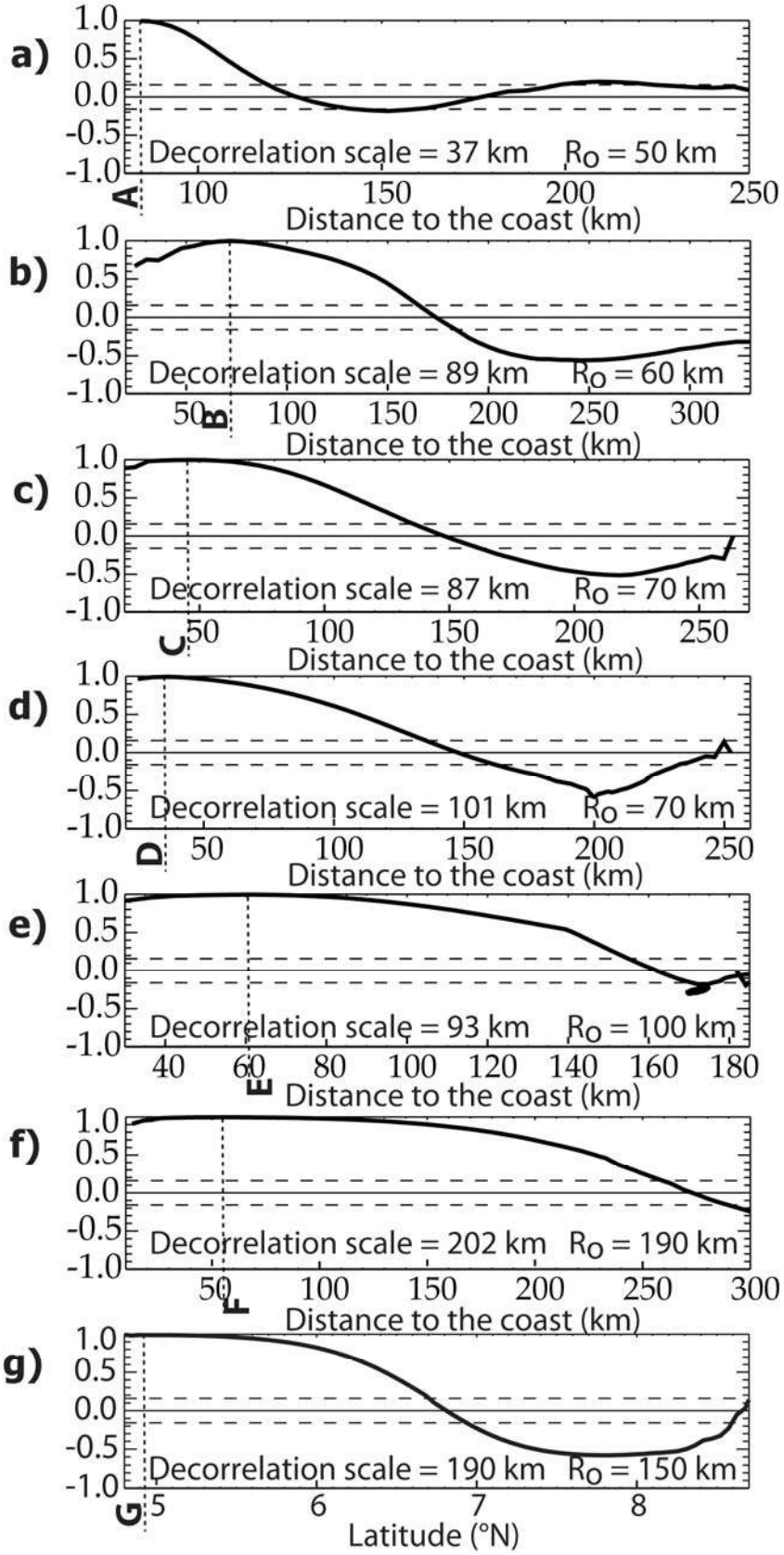
a)
Decorrelation scale = 37 km
R_O = 50 km
A
Distance to the coast (km)
b)
Decorrelation scale = 89 km
R_O = 60 km
B
Distance to the coast (km)
c)
Decorrelation scale = 87 km
R_O = 70 km
C
Distance to the coast (km)
d)
Decorrelation scale = 101 km
R_O = 70 km
D
Distance to the coast (km)
e)
Decorrelation scale = 93 km
R_O = 100 km
E
Distance to the coast (km)
f)
Decorrelation scale = 202 km
R_O = 190 km
F
Distance to the coast (km)
g)
Decorrelation scale = 190 km
R_O = 150 km
G
Latitude (°N)

Fig.11

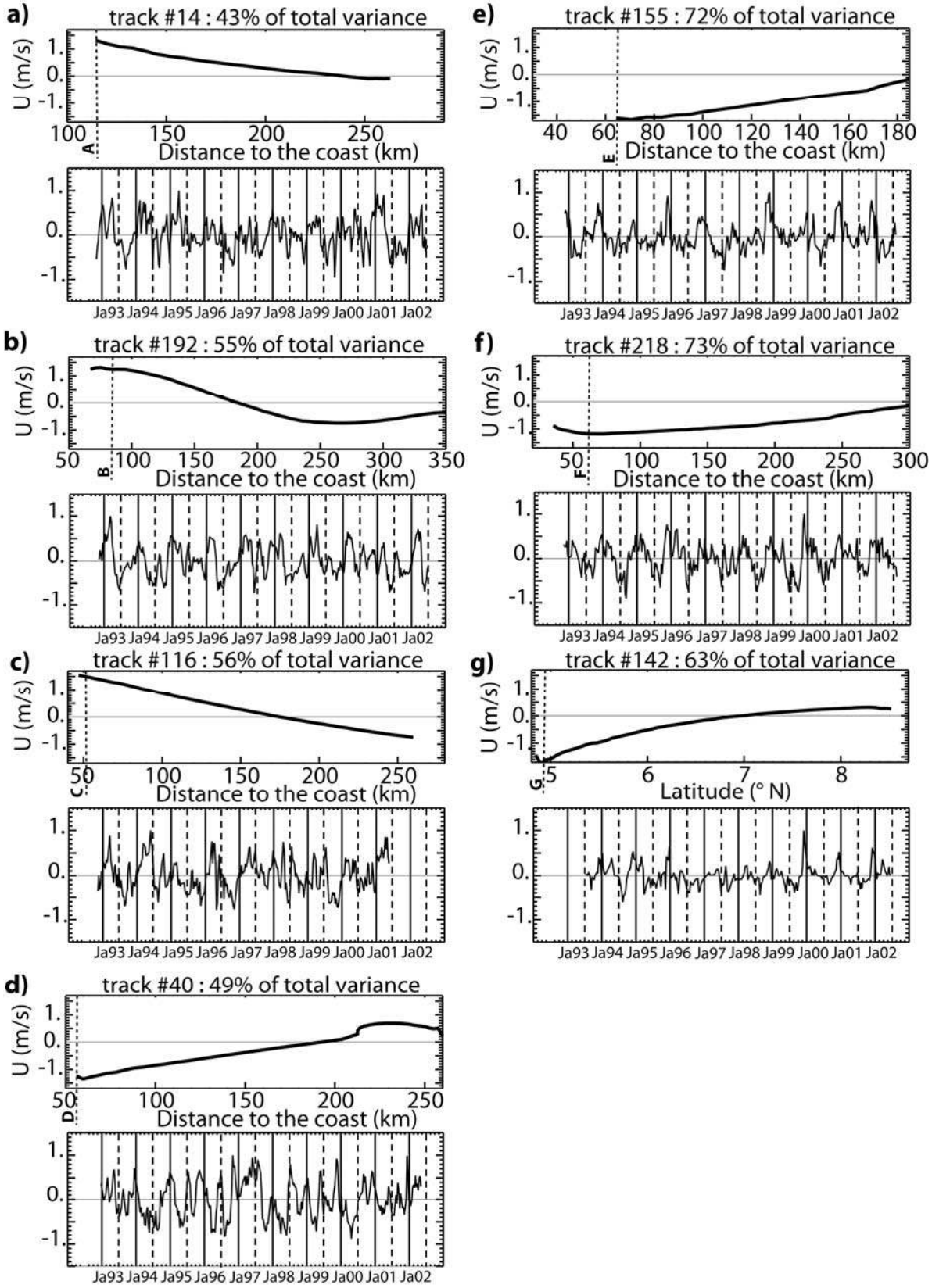
a)
track #14 : 43% of total variance
U (m/s)
A
Distance to the coast (km)
b)
track #192 : 55% of total variance
B
c)
track #116 : 56% of total variance
C
d)
track #40 : 49% of total variance
D
e)
track #155 : 72% of total variance
E
f)
track #218 : 73% of total variance
F
g)
track #142 : 63% of total variance
G
Latitude (° N)
Ja93 Ja94 Ja95 Ja96 Ja97 Ja98 Ja99 Ja00 Ja01 Ja02

Fig.12

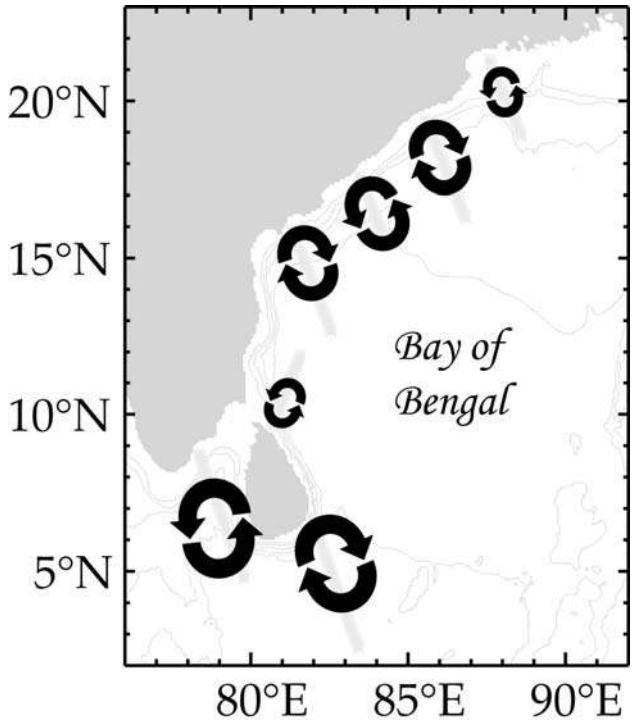
20°N
15°N
10°N
5°N
80°E
85°E
90°E
Bay of
Bengal

Fig.13

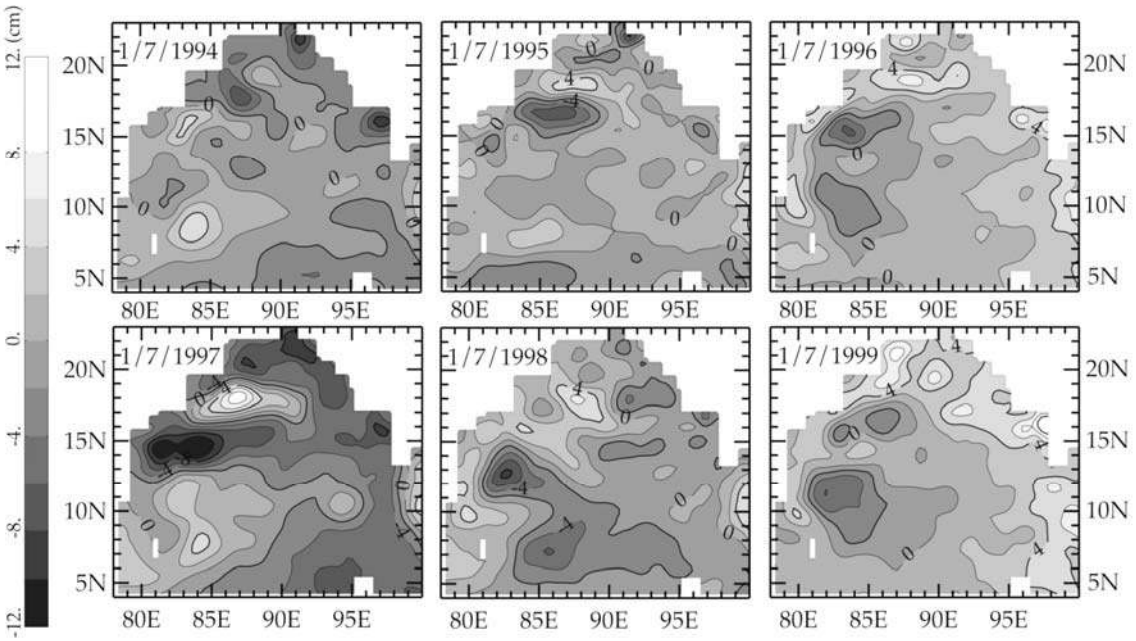
12. (cm)
8.
4.
0.
-4.
-8.
-12.
1/7/1994
1/7/1995
1/7/1996
1/7/1997
1/7/1998
1/7/1999
20N
15N
10N
5N
80E
85E
90E
95E

Fig.14

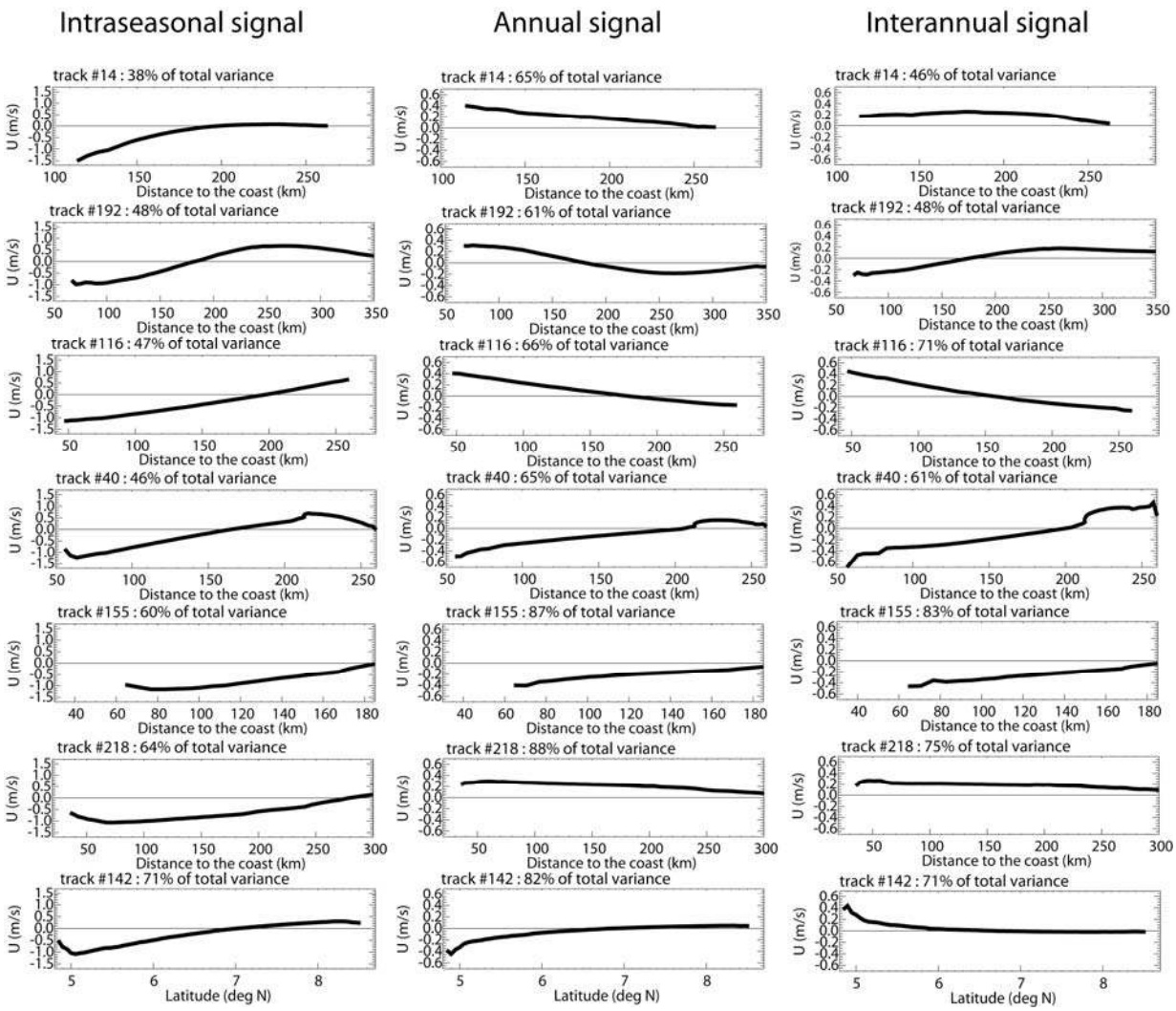
Intraseasonal signal
Annual signal
Interannual signal
track #14 : 38% of total variance
track #14 : 65% of total variance
track #14 : 46% of total variance
track #192 : 48% of total variance
track #192 : 61% of total variance
track #192 : 48% of total variance
track #116 : 47% of total variance
track #116 : 66% of total variance
track #116 : 71% of total variance
track #40 : 46% of total variance
track #40 : 65% of total variance
track #40 : 61% of total variance
track #155 : 60% of total variance
track #155 : 87% of total variance
track #155 : 83% of total variance
track #218 : 64% of total variance
track #218 : 88% of total variance
track #218 : 75% of total variance
track #142 : 71% of total variance
track #142 : 82% of total variance
track #142 : 71% of total variance
U (m/s)
Distance to the coast (km)
Latitude (deg N)

Fig.S1

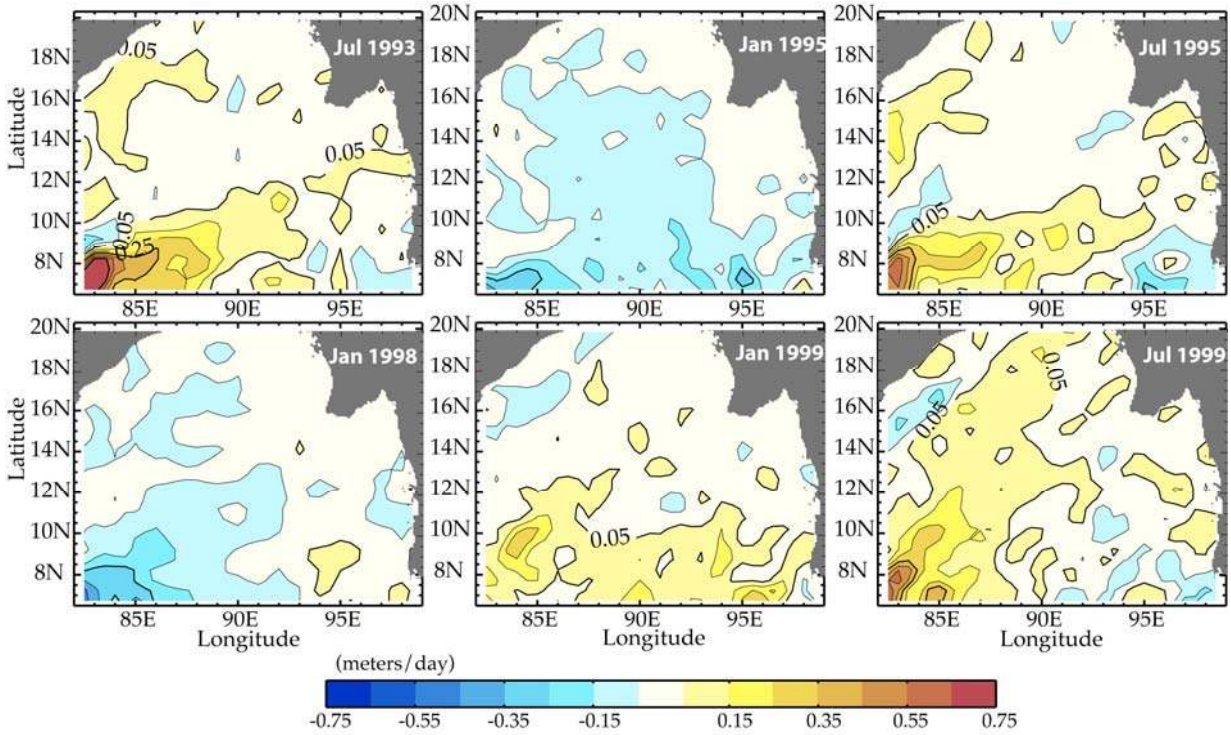
Jul 1993
Jan 1995
Jul 1995
Jan 1998
Jan 1999
Jul 1999
0.05
0.25
Latitude
Longitude
20N
18N
16N
14N
12N
10N
8N
85E
90E
95E
(meters/day)
-0.75
-0.55
-0.35
-0.15
0.15
0.35
0.55
0.75

Fig.S2